7-3-2012

Mechanical and electrical properties of carbon nanotubes surface-stamped on polydimethylsiloxane for microvalve actuation

Jeffrey Salzbrenner

Jeffrey Salzbrenner
Candidate

MECHANICAL ENGINEERING
Department

This thesis is approved, and it is acceptable in quality and form for publication:

Approved by the Thesis Committee:

Dr. Tariq Khraishi , Chairperson

Dr. Christopher Apblett

Dr. Yu-Lin Shen

MECHANICAL AND ELECTRICAL PROPERTIES OF CARBON NANOTUBES SURFACE-STAMPED ON POLYDIMETHYLSILOXANE FOR MICROVALVE ACTUATION

BY

JEFFREY SALZBRENNER

B.S., UNIVERSITY OF PORTLAND, 2008

THESIS

Submitted in Partial Fulfillment of the
Requirements for the Degree of
Master of Science

Mechanical Engineering

The University of New Mexico
Albuquerque, New Mexico

May, 2012

Acknowledgements

This thesis would not have been possible without the help and support of a great many people. It is a pleasure to thank those who made this possible.

My deepest gratitude goes to my advisors, Dr. Christopher Apblett and Dr. Tariq Khraishi, for their guidance, understanding, patience, and friendship during my graduate studies. Their ability to let me explore on my own, but at the same time provide the guidance to recover when my steps faltered, has been invaluable. Thanks also for reading previous drafts of this thesis and providing many valuable comments that improved the presentation and contests of this work.

I would like to thank my colleagues at the Advanced Materials Laboratory for providing valuable help and insight during my research. I would especially like to thank Adam Cook, Dr. Kyle Fenton, and Eric Branson for their assistance and support, as well as providing much needed humor and entertainment in the lab.

I would also like to thank the Department of Mechanical Engineering at the University of New Mexico, especially those members of my thesis defense committee: Dr. Apblett, Dr. Khraishi, and Dr. Shen. Also thanks to Sandia National Laboratories for their support of this research.

Finally, and most importantly, I would like to give my deepest thanks to my friends and family, whose love, support, and faith in me have made this possible. Thanks to my fiancé, Christine, for her unwavering love, support, understanding, and patience over the last few years. My parents, Shirley and Dick, receive my deepest gratitude and love for their dedication, support, and love.

MECHANICAL AND ELECTRICAL PROPERTIES OF CARBON NANOTUBES SURFACE-STAMPED ON POLYDIMETHYLSILOXANE FOR MICROVALVE ACTUATION

BY

JEFFREY SALZBRENNER

ABSTRACT OF THESIS

Submitted in Partial Fulfillment of the
Requirements for the Degree of
Master of Science

Mechanical Engineering

The University of New Mexico
Albuquerque, New Mexico

May, 2012

Mechanical and Electrical Properties of Carbon Nanotubes Surface-Stamped on Polydimethylsiloxane for Microvalve Actuation

By

Jeffrey Salzbrenner

B.S., Mechanical Engineering, University of Portland, 2008

M.S., Mechanical Engineering, University of New Mexico, 2012

Abstract

I report on the study of the electrical and mechanical effects of the inclusion of a thin layer of multiwalled carbon nanotubes (MWCNT) into the surface of polydimethylsiloxane (PDMS) as a method of creating an electrically actuated, flexible microfluidic valve. Samples of PDMS loaded with various surface loadings of MWCNT on the surface are prepared and tested using a uniaxial tension tester, combined with a four point probe electrical test. In contrast with other works reporting inclusion of MWCNT in the bulk of the material, I have found that inclusion of the MWCNT on the surface only has no discernable effect on the mechanical properties of the PDMS samples, but causes a significant and repeatable change in the electrical performance. I have also found that a loading of 4.16 g/m^2 results in an electrical resistivity of $7.31 \cdot 10^{-4}$ ohms·cm, which is 200% lower than that previously reported for bulk inclusion samples. The microstructure of the MWCNTs was found to consist of both individual fibers and spherical clumps of fibers. I suggest that, due to the microstructure of the MWCNTs used in this study, the mechanical properties can be modeled as a thin layer of particulates, while the electrical properties can be modeled as a thin bed of bulk MWCNTs.

Table of Contents

List of Figures

List of Tables

1. Introduction

Microfluidic systems control and transport reagents and fluids in compact devices by integrating multiple components. Of these components, one of the most useful is the microvalve, which allows switching of microfluidic flows. A standard design includes a channel entering a valve seat, in which the fluidic path is opened or closed by deformation of a membrane [1]. Microvalves are actuated by various methods, and are broadly classified as either active or passive. Passive microvalves do not require an external input in order to achieve actuation, and two examples are a check valve and ball valve [1, 2]. Active microvalves, on the other hand, require an external input to induce actuation. Two common methods of producing actuation in active microvalves are pneumatic [3, 4, 5] and electrostatic [6].

One of the more common designs of pneumatic microvalves is based on pressure actuation of the polymer membrane [4]. These valves have large deflection capabilities, but suffer from having large externally applied pressure systems that are difficult to miniaturize. Alternatively, many electrostatically actuated valves can be actuated with a simple potential applied across the channel, but suffer from low displacements and difficult fabrication processes, as well as leakage [1, 6]. Optimally, one would like to have the flexibility and deflection distance of the pressure driven systems, but with the ease of integration of the electrostatic systems, which would require the addition of a flexible conductive layer to the flexible membrane [7, 8, 9]. One method to achieve this is to add a conductive filler to the microvalve membrane.

A large deflection of the membrane compared to the channel height is necessary for opening and closing the valve. Recently, silicone elastomer has been used for microvalve

membranes due to its low Young's modulus and good sealing properties [10, 11]. In particular, polydimethylsiloxane (PDMS) has been used previously as the material for microvalve membranes and channels [10, 12, 13] due to its excellent properties for use in microfluidics. PDMS is a heat promoted curable polymer (thermoset) that consists of a pre-polymer (base) and a cross-linker (curing agent). Khanafer, Duprey, and Schlict [14] studied the effects different mixing ratios and strain rates have on the mechanical properties. They used five different base to crosslinker mixing ratios (6:1-10:1) and found that as the mixing ratio increases, the elastic modulus increases, but only up to a ratio of 9:1, after which the elastic modulus starts to decrease with increased mixing ratio.

Liu et al. [11] looked at the influences of curing temperature on the mechanical properties of PDMS and found that PDMS has two different deformation regions within its stress-strain curve. The first region is more linear with a smaller slope, while the second region (starting at about 200% elongation) has a larger slope, meaning that a larger force is needed to cause the same amount of elongation. This is believed to be due to work hardening, where polymer chains start slipping, absorbing some of the applied mechanical work. However, this result was not reported with others [14, 15, 16]. Liu el al. also found that the mechanical properties of PDMS are independent of heating time at low cure temperatures. However, at higher cure temperatures (above 200 ^{o}C) there is an evident decrease in the mechanical strength of PDMS. Higher cure temperatures were also found to yield lower mechanical strength compared to samples tested at lower cure temperatures. This decrease in strength is believed to be due to thermal decomposition, which starts at around 200 ^{o}C in PDMS.

Since their discovery in 1991by Iijima [17], carbon nanotubes (CNTs) have been used in conjunction with other materials to form nanocomposites. Others [15, 16, 18, 19, 20, 21] have used the high strength, stiffness, flexibility, resilience, and conductivity of CNTs to increase the properties of polymers. This, along with their low density and high aspect ratio, make CNTs ideal reinforcing agents. In particular, multiwalled carbon nanotubes (MWCNTs) have different properties than single walled carbon nanotubes (SWCNTs) due to the differences in manufacturing. MWCNTs have high electrical conductivity and current density along their axis. In SWCNTs, conductivity depends on the chirality of the graphene sheet, while MWCNTs are reported to always be electrically conductive. However, the successful implementation of CNTs (both SWCNTs and MWCNTs) in polymers also requires controlling the dispersion of CNTs to ensure uniform and consistent composites [19]. This can be done a number of ways, including using surfactants to help with dispersion [8, 19].

Mathur et al. [19] used MWCNTs to reinforce the thermoplastic polymers polymethyl methacrylate (PMMA) and polystyrene (PS). The composites showed increased conductivity with increased nanotube content. It was also found that the addition of MWCNTs in PMMA and PS caused fracture to change from ductile to brittle. Stiffness and elastic modulus also increased, while the increase in tensile strength was reported as low. Differences between functionalized and non-functionalized MWCNTs were also examined, and it was observed that the functionalized CNTs resulted in improved strength compared to non-functionalized CNTs.

A few others [15, 16, 18] have added carbon nanotubes directly into the bulk of PDMS and looked at the mechanical and electrical properties of the composite, although

not simultaneously. Wu et al. [15, 16] mixed different weight ratios (up to 4.0 wt%) of MWCNTs with PDMS and found that the elastic modulus and strength of the nanocomposites increased with increased content of CNTs. Increased CNT content also resulted in increased brittleness compared to pure PDMS. Additionally, higher curing temperatures resulted in improved mechanical properties of the PDMS/CNT nanocomposites. Wu et al. [16] also found that the electrical resistance of PDMS improved with the addition of CNTs, observing that the resistance of PDMS/CNT composites decreases two orders after the addition of 2.0 weight percent of CNTs. However, the resistivity of composites was only recorded to be as low as 10^{12} Ω·cm, which is quite high when compared to resistivity of elemental carbon (0.001375 Ω·cm) [22].

Liu and Choi [8] studied the electrical effects of thin layered CNTs on PDMS for flexible, patterned MEMS devices. In this study, a thin layer of PDMS/CNT composite was added onto bulk PDMS. It was discovered that as the CNT weight percentage increased in the composite, the conductivity increased. Samples ranging from 3 to 15 weight percent of CNTs were studied, with resistivities ranging from 33,333 Ω·cm to 15.87 Ω·cm. When compared to elemental carbon (0.001375 Ω·cm), this is again quite high, due to the fact that the PDMS acts as an insulator. It was speculated that an applied electric field may align the CNTs inside the PDMS in a direction parallel to the electric field. Mechanical testing was not performed. However, based on the mechanical testing discussed above, it is expected that the mechanical properties of the composites would be much stiffer and stronger than that of pure PDMS.

Kim et al. [9] used a photolithography method to pattern CNTs on the surface of PDMS. CNT layers ranging from ~700 to ~1300 nm where achieved, with a resistivity as low as 0.013 Ω·cm at the thickest layer. This is about an order of magnitude higher than elemental carbon (0.001375 Ω·cm). The mechanical effects that this surface layering method has on the composite was not studied in this work.

As noted earlier, large deflections of the microvalve membrane are necessary to open and close the microchannel, and the addition of CNTs into the bulk of the PDMS can cause the resulting composite to become quite stiff. This in turn causes the membrane to require more energy in order to actuate, which is generally undesired. In order to avoid large mechanical changes in the PDMS, a surface-stamping method in which the CNTs are applied to the top surface of the PDMS is studied in this work. It is thought that this method might not have as drastic an effect on the mechanical properties of the PDMS while still providing a conductive layer.

This thesis describes the incorporation of CNTs imprinted on the surface of PDMS as a method for increasing electrical conduction for use in electrostatic microvalves. Here, I present the results of mechanical deformation on a CNT/PDMS composite, and measure the mechanical and electrical response of the nanocomposite in-situ. This work represents for the first time coupled mechanical and electrical behavior of surface-loaded PDMS/CNT composites. Correlations between these two behaviors are directly made.

2. Experimental

2.1 Material Preparation

RTV615 Silicon Rubber Compound (Momentive Performance Materials RTV615A&B, Columbus , OH) was used for the matrix, and came in two components that had to be mixed: a base and a crosslinker. A ratio of 10:1 base to crosslinker was measured and mixed in a high shear mixer (THINKY AR-100, Tokyo, Japan) for 3 minutes and defoamed for another 2 minutes to ensure homogeneous mixtures. The RTV615 compound is referred to as PDMS in this paper.

Multiwalled carbon nanotubes (MWCNT, 6-9 nm diameter, ~1000 aspect ratio, SouthWest NanoTechnologies Inc, Norman, OK) were used as the conductive filler. In order to achieve a randomly oriented and even distribution of CNTs, a solution of CNTs (50 mg MWCNT: 500 mg sodium dodecyl sulfate (SDS): 50 mL distilled H_2O) was deposited on a filter. The CNT solution was sonicated using an ultrasonic cleaner (Fisher Scientific FS30D, Waltham, MA) for 1 hour and the surfactant SDS served to keep the CNTs suspended in the solution during filter preparation. A pipette was used to transfer different volumes (2 – 8 mL) of the CNT solution into 100 mL of distilled water and filtered through a Durapore membrane filter (Durapore 0.22 µm pore, Millipore, Billerica, MA) with a vacuum pump and rinsed with ethyl alcohol to ensure that all the SDS was rinsed through the filter. This resulted in a layer of uniform, randomly distributed CNTs on the filter. The amount of CNTs on the filter could be adjusted by adding different amounts of the CNT solution onto the filter. See Figure 1 for a schematic of the process.

2.2 Sample Preparation

PDMS/CNT composites were made by transferring the filtered CNTs onto semi-cured PDMS samples. The CNT stamping method used by Mohan et al. [23] was employed to transfer the CNTs onto the PDMS. The 10:1 base to crosslinker mixture of PDMS was poured into a wax mold (96x25 mm, 1.5 mm thickness) and semi-cured in an oven at 70^{o}C for 1 hour. A vacuum was pulled on the oven for the first 5 minutes to eliminate any trapped air bubbles in the compound. The semi-cured PDMS was then removed from the mold and stamped into a tension testing sample using a die-punch (Texas Custom Dies, INC, Mansfield, TX) that followed ASTM standard D412 [24]. The gauge length and gauge width of the test sample was 26 mm and 2.5 mm, respectively. Figure 2 shows a picture of the dogbone sample and its dimensions. The PDMS sample was weighed (Mettler-Toledo, Inc AB204-S/FACT, Columbus, OH) and the CNT filter was stamped on one side. The PDMS/CNT composite sample was then weighed again, so an accurate weight of CNTs on each sample was known. The composite was then placed back in the oven for an additional hour to fully cure. Twelve (12) to fourteen (14) composite samples were made at once from each batch of PDMS, and three (3) to five (5) samples were left as 'blank' PDMS with no CNTs as a control group. In order to have accurate measurements of the sample dimensions for stress calculations, width and depth measurements were taken using an optical microscope (Nikon SMZ1000, Tokyo, Japan) with an Infinity1 camera and Infinity Analyze software (Lumenera Corporation, Infinity 1-3, Ottawa, Ontario, Canada) along the gauge length. A depiction of the CNT transfer process can be seen in Figure 1.

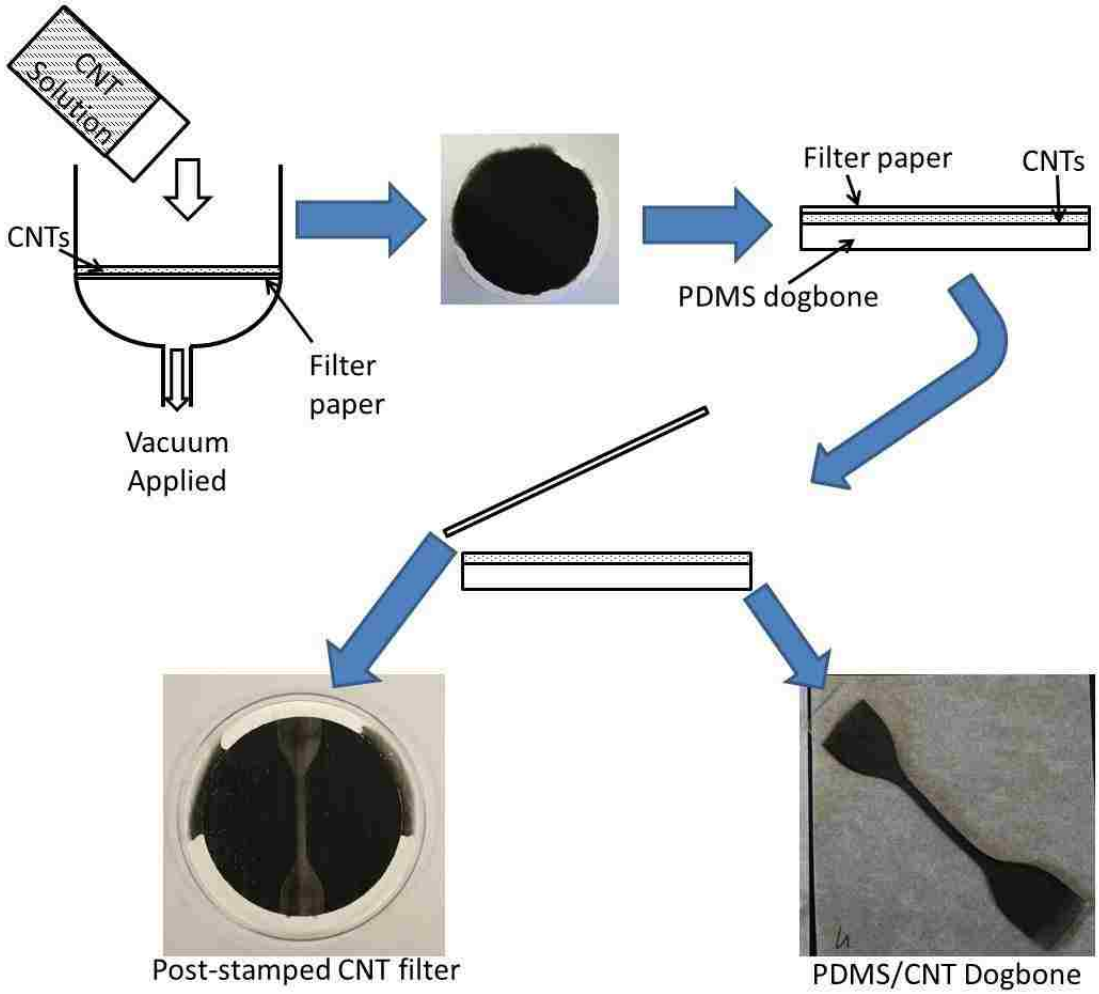

Figure 1. Diagram of CNT transfer process.

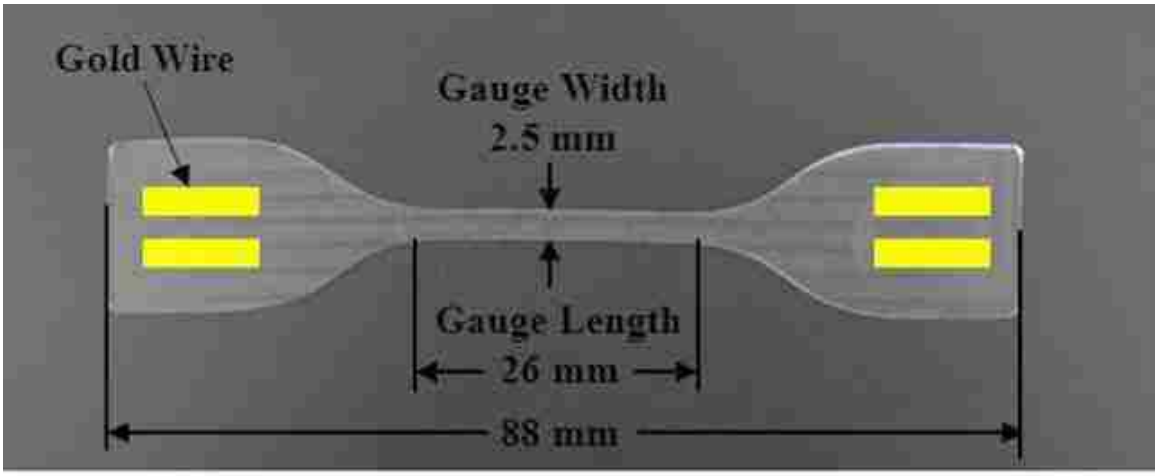

Figure 2. Dogbone sample and dimensions used for stamping PDMS.

2.3 Tension Testing Setup and Calibration

The specimens were tested in tension using a custom made robot that could move in the X,Y, and Z axis with an accuracy of 15 μm and a repeatability between 5-10 μm. A load cell (Transducer Techniques MDB-10, Temecula, CA) with a capacity of 10 pounds was used to record the tension force. An amplifier/conditioner module (Transducer Techniques TMO-1) was used to convert the signal from the load cell to a computer. Each specimen was connected to a multimeter (Fluke 45 Dual Display Multimeter, Everett, WA) at the grip interface using gold wire in order to record the resistance throughout the tension test using a 4-wire resistance test (see Figures 2 and 3 for approximate placement and wire set-up). To ensure all samples were gripped with an even clamping force, a torque screwdriver was used to apply 4 inch-pounds of force to the screws of each grip. The samples were tested at a strain rate of 0.01 mm/s. The voltage and resistance were recorded throughout the sample displacement using LabView software. Figure 3 shows a schematic of the testing setup. The voltage of the load cell

was converted into a force using the specifications from the load cell, and the stress and strain of the sample was calculated using the definition of engineering stress,

$$\sigma = F/A \tag{1}$$

and engineering strain,

$$\varepsilon = \Delta l/l \tag{2}$$

where F is the applied force, A is the original cross-sectional area of the sample, l is the original length of the sample, Δl is the change in sample length. The measurements using the Infinity Analyze software were used to calculate the cross-sectional area of each sample. The CNT area density of each sample was calculated using the equation

$$A_d = W_{cnt}/A_s \tag{3}$$

where A_s is the surface area of the sample and W_{cnt} is the weight of the CNTs on each sample. The percent weight of CNTs on each sample was calculated using

$$Wt.\%\ CNT = W_{cnt}/W_t \tag{4}$$

where W_t is the total weight of the sample that is covered by CNTs (i.e. weight of the CNTs plus PDMS covered by CNTs).

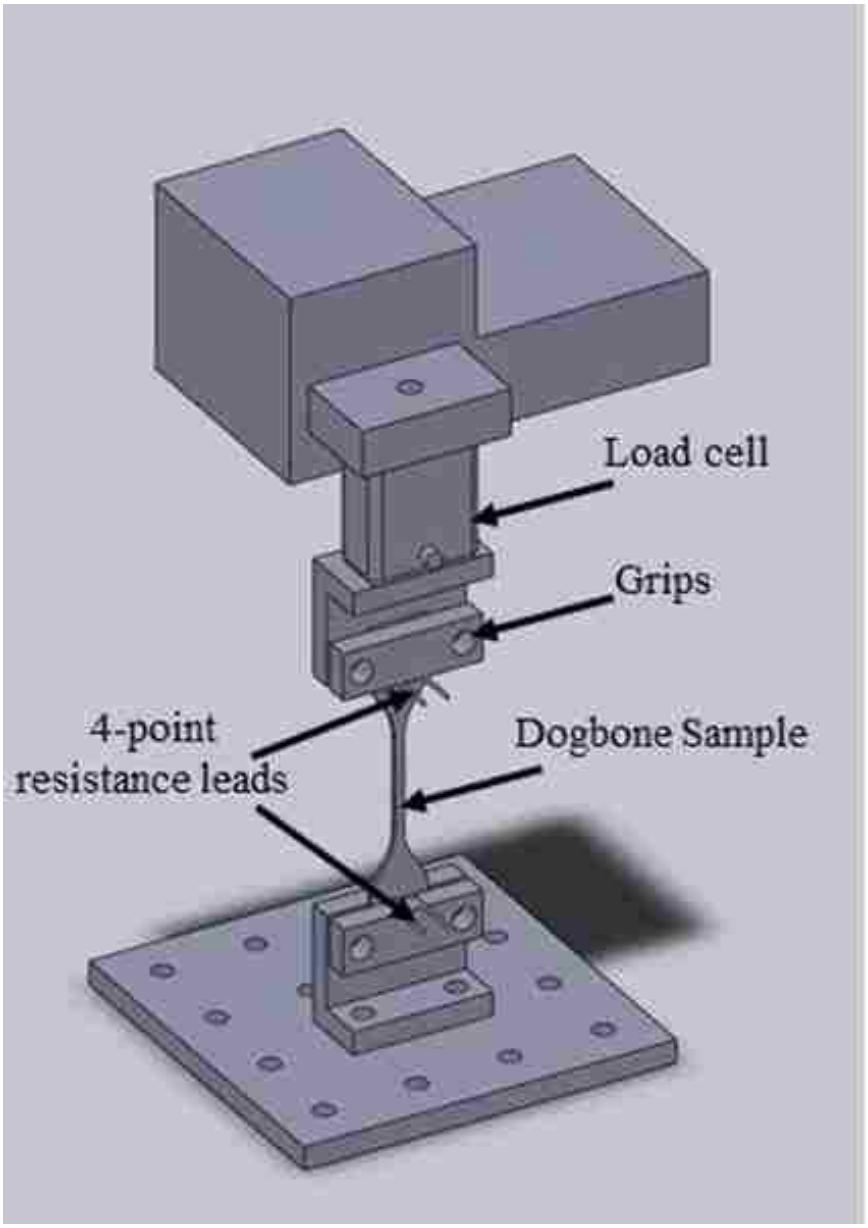

Figure 3. Schematic of the testing setup

To ensure that the load cell and robot were functioning and recording data properly, samples of pure PDMS tested using the custom tension testing machine were compared to samples tested using a calibrated Instron machine. The results can be seen in Figure 4. The curve of the sample tested using the custom tension testing robot closely follows the

curve of the sample tested on the Instron machine, signifying that the force and displacement recorded using the custom tension testing robot are accurate.

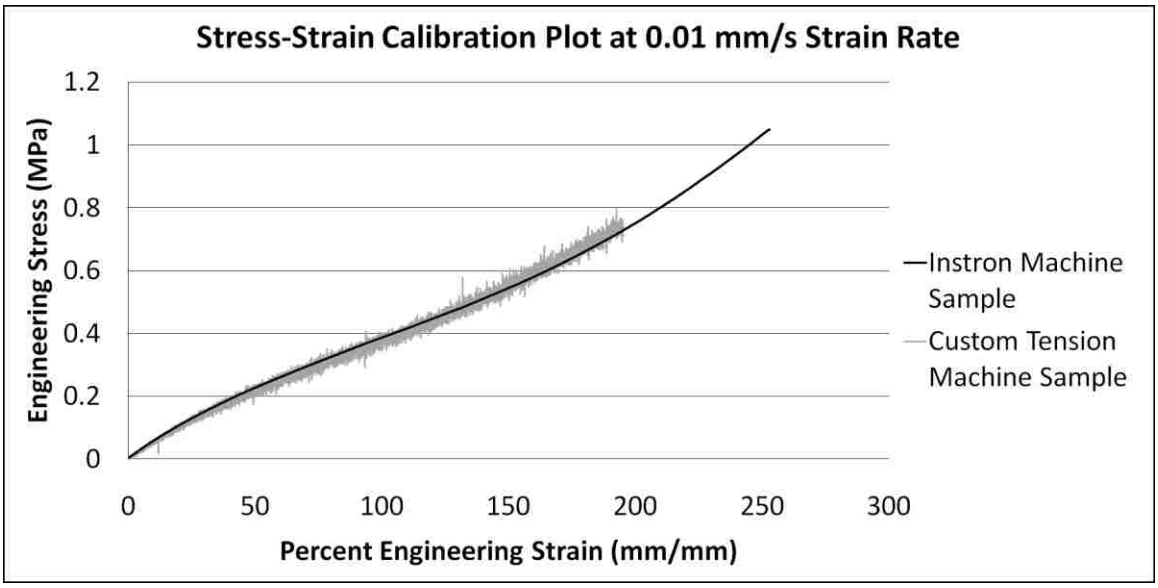

Figure 4. Stress-Strain Comparison with Instron

The noise seen in the custom-built tension machine used for these experiments is due to the use of a brushed servo motor for displacement. The brushed servo motor steps through the displacement, resulting in small 'jumps' in the voltage that the load cell records. To smooth out the noise of the data, a Gaussian kernel regression was applied [25, 26]. A kernel regression is a non-parametric regression method that does not assume an underlying distribution of the data (such as a normal distribution). The kernel regression assigns a set of identical weighted functions called kernels to each data point, which assigns a weight to each location based on its distance from other data points. For a given data set (X_i, Y_i), a regression function $\hat{f}(x)$ is found that is a best-fit to the data. The regression fits the data to the equation $Y_i = \hat{f}(X_i)$, where:

$$\hat{f}(x) = \frac{\sum_{i=1}^{n} K(\frac{x-X_i}{h})Y_i}{\sum_{i=1}^{n} K(\frac{x-X_i}{h})} \quad (5)$$

where *h* is the bandwidth (a smoothing parameter) and K is the kernel. In this case, a Gaussian kernel regression is used, where:

$$K = \frac{1}{\sqrt{2\pi}} e^{-\frac{x^2}{2}} \quad (6)$$

For each data point, the Gaussian kernel is applied over the entire X domain, and at each x position, the estimated $\hat{f}$ is calculated. The bandwidth works as a smoothing function and gives weights to other data points around it. Figure 5 illustrates the result of applying the Gaussian kernel regression to one of the data sets. From this point forward, the stress-strain data will be shown with a Gaussian kernel regression applied, and calculations for the elastic modulus will be made with the Gaussian kernel regression data [25, 26].

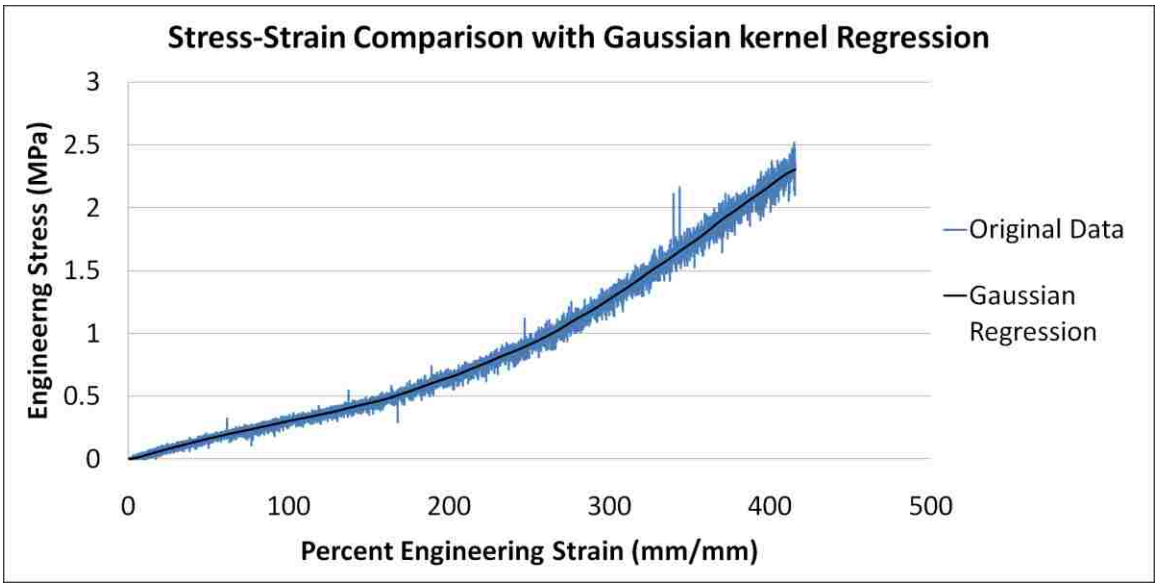

Figure 5. Original Data with Gaussian kernel regression applied

Tests were also run to ensure that the 4-point resistance set-up was functioning correctly. The resistance of gold wire (Alfa Aesar, Premion Gold Wire, 0.5 mm diameter, 99.9985% pure, Ward Hill, MA) was measured, and the resistivity calculated. This was compared to published results for the resistivity of gold. The measured resistivity was 2.36×10^{-8} Ω·m and the published resistivity was 2.33×10^{-8} Ω·m [27]. The percent error is 1.28%. See Appendices A and B for preliminary sample preparation methods and design iterations of the dogbone shape and machine grips.

3. Results and Discussion

3.1 Mechanical

3.1.1 Pure PDMS

Figure 6 shows the stress-strain curves of pure PDMS samples from the same batch of PDMS. Samples from the same batch mean that they were mixed, placed in the oven, and cured at the same time. All samples from the same batch have very similar stress-strain curves and are very consistent from sample to sample. PDMS exhibits a typical two region stress-strain curve. The first region is more linear and has a smaller slope than the second region. The second region has a larger slope (a larger stress is required to produce the same amount of strain). This larger force required for deformation is due to the polymer chains slipping and absorbing some of the mechanical work, and is typically referred to as the work hardening effect [11, 28]. As seen in Figure 6, the transition from the first region to the second region occurs at around 150% strain. This agrees with Liu et al. [11], who also found that the transition between the two regions of PDMS also occurs at around 150-200% strain.

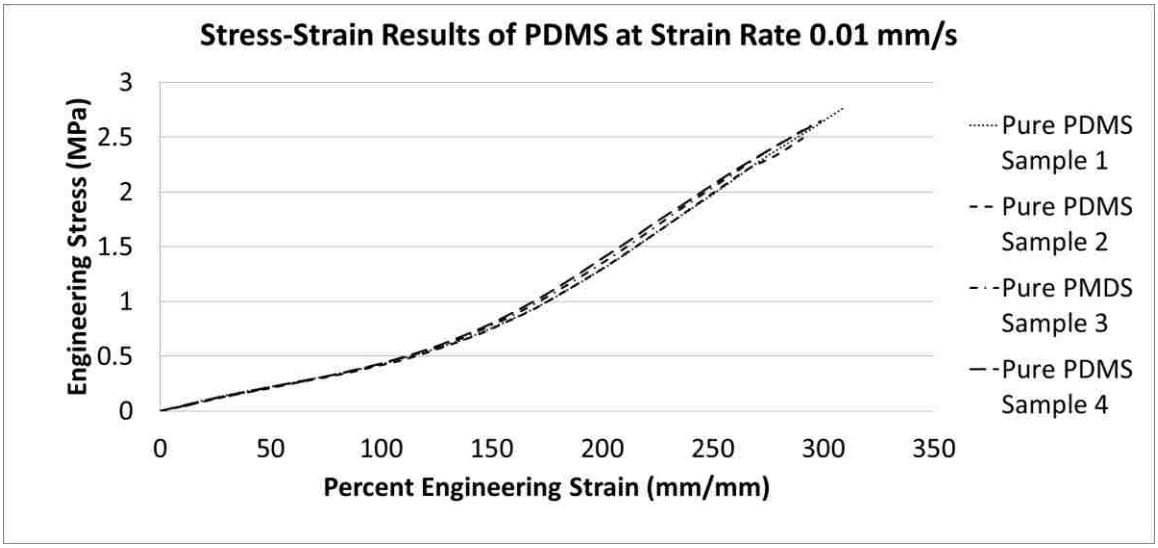

Figure 6. Pure PDMS stress-strain data from same batch

The elastic modulus ($E = \sigma/\varepsilon$) was calculated using a linear least squares fit from 0 to 100 % strain. The elastic modulus describes the stiffness of a material. The average modulus of the samples from Figure 6 is 0.42 MPa. The similar stress-strain plot of samples from the same batch indicates that the test procedure and results are highly reproducible and repeatable.

While the stress-strain curves of PDMS from the same batch have similar stress-strain profiles, samples from different batches have slightly different stress-strain profiles. Figure 7 shows a plot of the typical curves from four different batches of PDMS. The variations between batches are attributed to small changes in the mixing ratio and oven curing temperatures.

Table 1 shows a comparison of the elastic modulus between several different batches from this work as well as other values from literature. The differences between different works are due to the many parameters that affect PDMS's material properties, such as base to crosslinker mixing ratio, curing temperature, curing time, and strain rate.

These parameters have been shown by others [14, 15, 16, 18] to affect the material properties of PDMS.

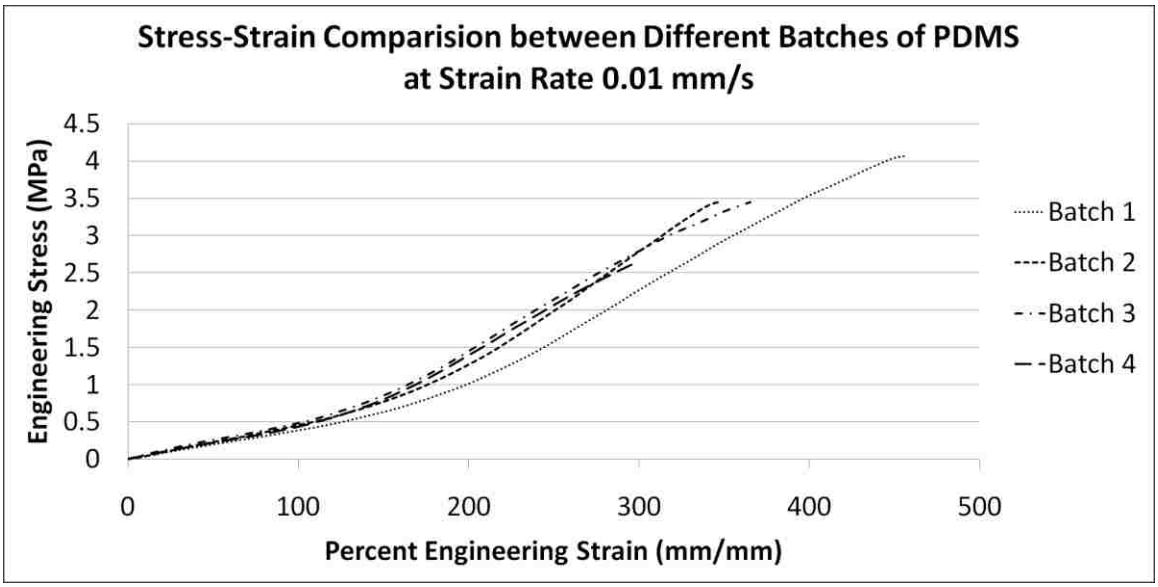

Figure 7. Stress-Strain Comparison between PDMS Batches

Table 1. PDMS Comparison

Result From	Curing Conditions	Strain Rate	Mixing Ratio	PDMS Batch	Elastic Modulus (MPa)
This Work	70°C for 2 hours	0.01 mm/s	10:1	Batch 1	0.39
				Batch 2	0.45
				Batch 3	0.47
				Batch 4	0.42
Khanafer et al [14]	65°C for 12 hours	5 mm/min	6:1	--	0.73
			7:1	--	1.15
			8:1	--	1.26
			9:1	--	1.51
			10:1	--	1.37
		500 mm/min	6:1	--	0.93
			7:1	--	1.2
			8:1	--	1.34
			9:1	--	1.53
			10:1	--	1.47
Wu et al. [15]	150°C for 15 minutes	1 mm/s	10:1	--	1.65
Wu et al. [16]	100°C for 1 hour	0.1 mm/s	10:1	--	1.05
	150°C for 15 minutes				1.32

3.1.2 PDMS/CNT Composite

Figure 8 shows the effects that the addition of CNTs has on the mechanical properties of PDMS. Composites with area densities ranging from 0.000 g/m^2 (pure PDMS) to 4.162 g/m^2 are plotted. As can be seen, composite samples have a similar stress-strain profile to that of pure PDMS. This indicates that the surface stamped CNTs do not have a noticeable effect on the mechanical properties of the composite. As the composites are strained, it can be seen that the plots are all initially aligned and have very similar stresses up to 125% strain. However, at strains above 125%, differences in the stress start to become more pronounced between the samples. The measurement variations do not correspond to any particular area density, and are therefore attributed to slight errors in the dogbone dimensions measured.

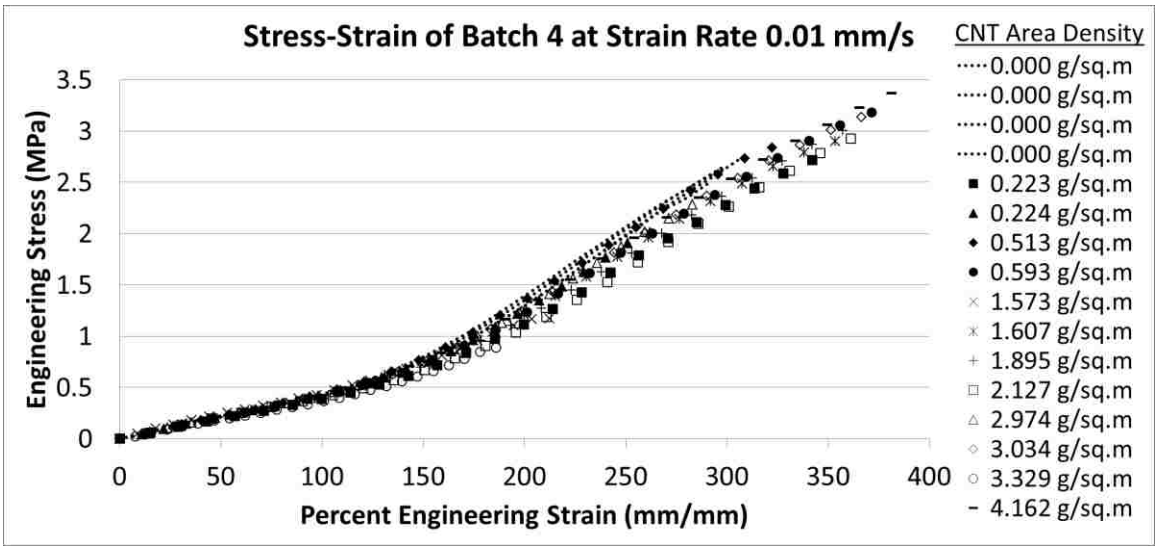

Figure 8. Stress-Strain plots of PDMS/CNT and pure PDMS samples

Due to the proposed application for the CNT/PDMS composites for use in microvalves, it is unlikely that strains greater than 100% will be seen. It is therefore useful to look at the elastic modulus of the composites. Figure 9 shows a plot of the elastic modulus versus the percent weight of CNTs for each sample from the previous figure. As expected from the stress-strain plot, the addition of CNTs have a negligible effect on the elastic modulus of the composites. The elastic modulus of surface stamped CNTs are compared to those of CNTs added to the bulk of PDMS in Table 2. The percent of CNTs added to the surface of the PDMS was limited by the amount that can 'stick' to the surface of the tacky PDMS during sample preparation. For this reason, weight percentages similar to those seen in studies examining the mechanical effects of bulk added CNTs could not be achieved with the surface stamping method used in this work. While the weight percentages of the two methods differ quite a bit, it can be anticipated that the addition of CNTs to the bulk of the PDMS can have a more significant effect on the mechanical properties of the composite.

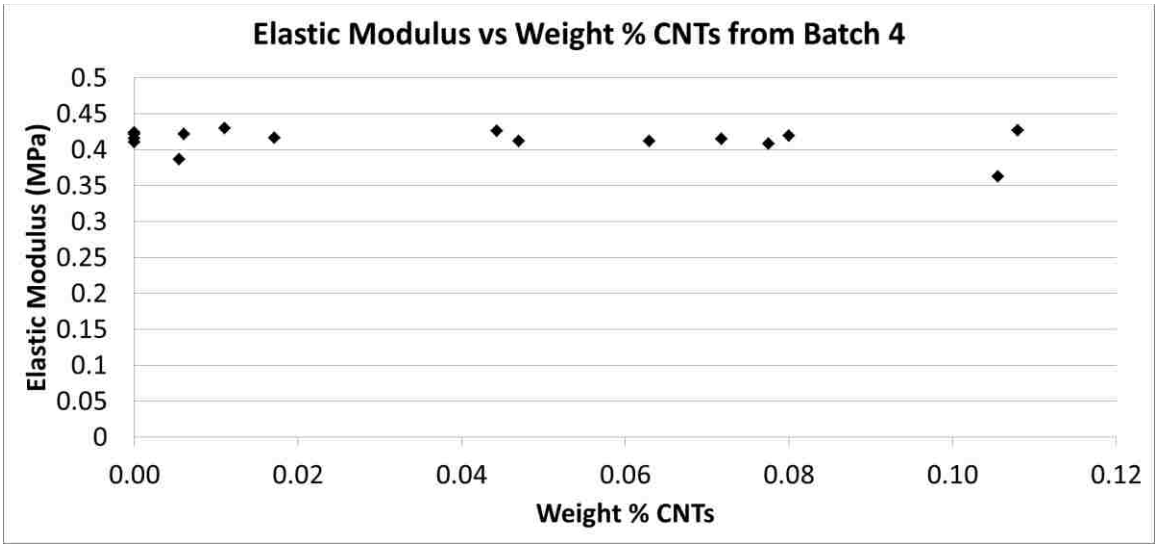

Figure 9. Elastic Modulus vs Weight Percent of CNTs

Table 2. Comparison of PDMS/CNT elastic modulus

Result From	Strain Rate	Curing Conditions	CNT Weight %	Elastic Modulus (MPa)	% Increase over pure PDMS
This Work	0.01 mm/s	70°C for 2 hours	0 - 0.11	0.42	--
Wu et. al. [15]	1 mm/s	150°C for 15 minutes	0	1.65	--
			1	1.71	3.64
			2	1.91	15.76
			4	2.34	41.82
Wu et. al. [16]	0.1 mm/s	100°C for 1 hour	0	1.05	--
			1	1.17	11.43
			2	1.1	4.76
			4	1.35	28.57
		150°C for 15 minutes	0	1.32	--
			1	1.41	6.82
			2	1.43	8.33
			4	1.54	16.67

3.1.3 Theoretical Mechanical Models

In order to understand why the surface stamped CNTs do not have an effect on the mechanical properties of the sample, it is important to understand some basics about composite theory. In this section, several composite models will be explored to see if they accurately predict the mechanical results achieved with the CNT surface stamped method. The basic Rule of Mixtures for composites states that the modulus of a composite is a volume weighted average of the moduli of the fiber and the matrix. The basic Rule of Mixtures model is intended for a composite with long continuous fibers oriented in the same direction. The Rule of Mixtures predicts an elastic modulus of

$$E_{c1} = E_{f1}V_f + E_mV_m \quad (7)$$

in the longitudinal direction and

$$1/E_{c2} = V_f/E_{f2} + V_m/E_m \quad (8)$$

in the transverse direction, where *E* is the elastic modulus, *V* is the volume fraction, and the subscripts *c, f, m, 1* and *2* denote the composite, fiber, matrix, longitudinal direction, and transverse direction, respectively [29]. While the basic Rule of Mixtures assumes that the fibers are as long as the specimen (so they are bearing a significant portion of the load during strain), Tsai and Pagano [29] modified the basic Rule of Mixtures model to incorporate composites with randomly oriented discontinuous fibers. Tsai and Pagano used the following equation for the average elastic modulus:

$$\tilde{E}_c = 3/8\,(E_1) + 5/8\,(E_2) \quad (9)$$

where E_1 and E_2 are the longitudinal and transverse elastic modulus of the composite obtained from the basic Rule of Mixtures. The volume of the matrix and fiber was calculated by using the average dimensions of the dogbone to get a volume of 1210.965 mm^3 for the matrix (assuming a depth of 1.5 mm) and 0.00605 mm^3 for the fiber (assuming a depth of 7.5 nm, the average diameter of the CNTs used). This gives a volume fraction of 0.999995 for the matrix and 0.000005 for the fiber. Using an elastic modulus of 0.00042 GPa (from Batch 4 used in this study) and 1000 GPa [30, 31, 32] for the PDMS and CNT, respectively, the Tsai and Pagano equation gives a theoretical elastic modulus of 2.29 MPa for the composite. The actual mechanical results give an average elastic modulus of 0.42 MPa for the composite. While this is much higher than what the actual mechanical results yielded, it is important to note that these equations where designed for fibers added to the bulk of the matrix. The Rule of Mixtures model also does not take into account the effect that the size of the fibers and the matrix-fiber

bond has on the composite. A model that takes into effect these conditions is therefore needed.

While the addition of fibers generally adds to the strength of the matrix, the fiber size can affect the load that is transferred from the matrix to the fiber. The fiber-matrix bond also plays an important role in the way the load is transferred throughout the composite [27, 33]. When a load is applied to the composite, it is transferred from the lower modulus matrix to the higher modulus fiber. This load transfer is more effective when a strong bond between the matrix and fiber exists. The load transfer ceases at the fiber ends, and the load is no longer transmitted from the matrix to the fiber. Long fibers are therefore the most effective for strengthening the matrix because more of the applied load is transferred to the higher modulus fibers. A critical fiber length exists for the most effective strengthening of the composite. This critical fiber length is dependent on the fiber diameter, fiber strength, and the strength of the fiber-matrix bond [33]. For fibers with lengths significantly less than the critical length, the matrix deforms around the fiber and the applied load is not effectively transferred to the fiber. Thus, for very small fibers, the matrix bears the major portion of the applied load, and the fibers act as particulates. Fukuda et al. [33] modified an equation used for fibers and used the following equation to predict the modulus of a composite with particulate reinforcements:

$$E_c = E_m[1 + (L + t)/4L]V_p + E_m(1 - V_p) \quad (10)$$

where L is the length of the particle perpendicular to the applied load, *t* is the length of the particle parallel to the loading direction, V_p is the volume fraction of the particulates, and E_m is the elastic modulus of the matrix. Using the values of 0.42 MPa for the elastic modulus of the matrix, a volume fraction of 0.000005 for the particulates, an *L* of 7.5 nm,

and a *t* of 7500 nm (CNT aspect ratio of 1000) gives a predicted elastic modulus of 0.4205 MPa for the composite. This gives approximately the same result as that of pure PDMS, and is similar to the results seen in the mechanical tests.

3.2 Electrical

3.2.1 CNT/PDMS Resistance

The recorded resistance was plotted versus the percent engineering strain. A curve fit was applied to the curve of each sample, and a 2^{nd} order polynomial was found to be the best fit for all the samples, with r^2 values ranging from 0.9924 to 0.9995. The resistance measurements during strain for samples from the same batch with the 2^{nd} order polynomial fit are shown in Figure 10. For each sample, the resistance increases with increased strain until infinite resistance is reached. However, the rate of change in resistance varies drastically with the area density of CNTs present. The change in resistance of samples with a higher area density of CNTs increases at a lower rate than samples with a smaller area density. Samples with a higher area density also have a lower initial resistance. It is hypothesized that the higher amount of CNTs present in samples with a higher area density creates more pathways for current to flow through. The high number of pathways present in these samples means that some of the pathways are redundant. This means that as the samples are strained, several pathways may get pulled apart, but others will still be able to carry the current, and thus the resistance changes at a much lower rate. The converse is also true: samples with fewer CNTs have fewer initial pathways, resulting in a higher initial resistance. Fewer CNTs also results in fewer pathways for current to travel, so when one pathway is broken, the current has to take a longer path across the sample, resulting in a greater increase in resistance per strain.

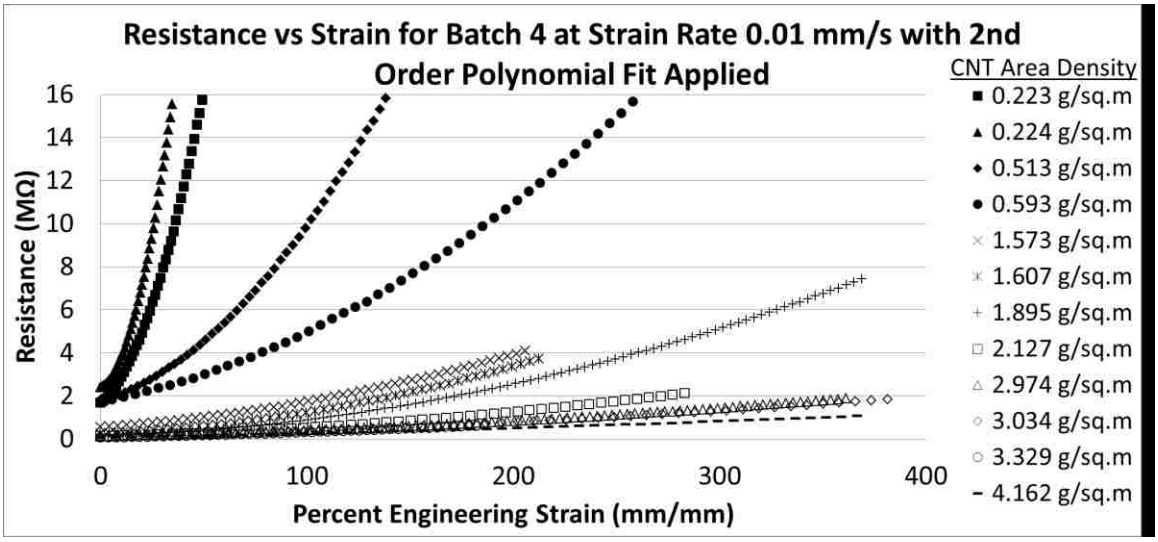

Figure 10. Resistance as a function of strain with a 2nd Order Polynomial Fit Applied

Figure 11 shows a plot of the initial resistivity as a function of CNT percent weight. Also plotted are the resistivity's for bulk carbon powder, graphite, and bulk MWCNTs measured using different resistance measurement methods [34, 35, 36]. As can be seen, the initial resistivity of the samples with a high area density of CNTs is lower than samples with a low area density. The resistance of the bulk MWCNTs and carbon powder for this comparison were all calculated assuming a bed of bulk particles 7.5 nm thick, 2.5 mm wide, and 63 mm long (the average diameter of the CNTs, approximate width of the samples, and approximate starting separation of the test leads, respectively). Modeling the CNTs as bulk powder gives a good approximation of the initial resistivity of the composite samples, and shows that the surface-stamped PDMS/CNT composites have resistivity on the order of bulk powders.

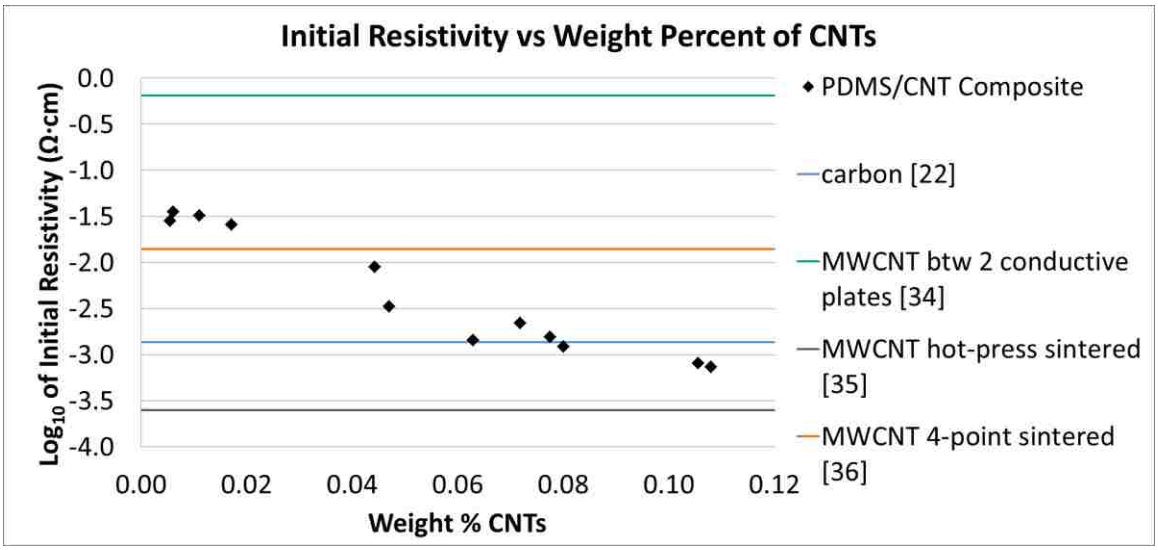

Figure 11. Initial Resistance vs. CNT % Weight

Just as the stress per strain changed with increased CNT weight percentage, the resistance per strain also changes with increased CNT weight percentage. Figure 12 shows a plot of the initial resistance per strain as a function of the weight percent of CNTs. The initial resistance per strain was calculated using a tangent method, where the derivative of 2nd order polynomial fit was taken at 0% strain. As can be seen, the higher the weight percent of CNTs on the composite, the lower the change in resistance. This is consistent with the hypothesis that samples with a higher area density have more electrically parallel pathways. The multiple pathways present in high loadings of CNTs allow for a lower sensitivity to strain, whereas at lower loadings, strain may be eliminating one of a few effective conductive paths, leading to a higher change in resistance with strain.

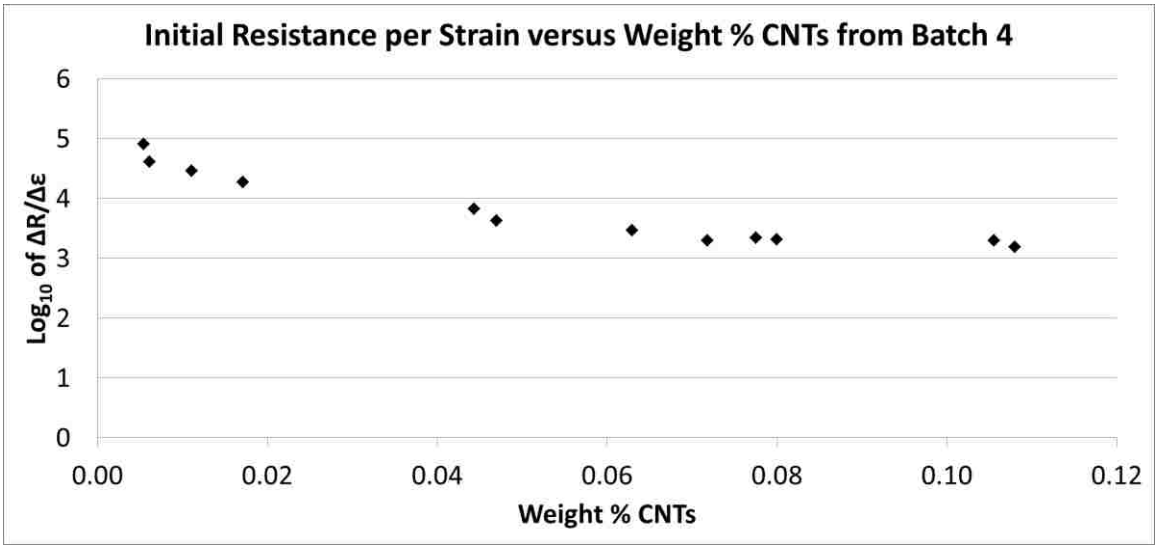

Figure 12. Resistance per strain versus CNT weight percent

3.2.2 Scanning Electron Microscopy

SEM images of several samples were taken to understand what is happening at the PDMS/CNT interface. This allowed for examination of the CNT layer and a better insight into the mechanical and electrical results. Figure 13 shows the SEM images of two samples, one with a high area density of CNTs and one with a low area density of CNTs. As can be seen, the sample with the low area density is much sparser than the sample with a high area density of CNTs. This corresponds with the plot of Figure 10, where samples with more area density have a lower initial resistance and a shallower slope. It also supports the hypothesis that the higher area density samples have more pathways for current to travel. Also of note in Figure 13 are the CNTs themselves. The CNTs are clumped into large spheres with individual CNT fibers connecting the 'spheres'. In order to discover whether or not this was a result of sample preparation, three different samples were imaged that were prepared using three different methods: one where the CNTs where put in a solution of H_2O and the surfactant SDS as described above, one where the

SDS was eliminated from the solution, and one where the CNTs were stamped directly onto the PDMS. The results indicate that the clumping of the CNTs was not a result of sample preparation, as all three preparation techniques show a clumping of the CNTs. It is therefore assumed that the clumping is a result of manufacturing or storage, and were received this way. While no direct testing was performed on the adhesion of CNTs to PDMS for each of the three transfer methods, it was noted through observation and handling that none of these methods seemed to produce increased adhesion. As seen in Appendix C, the amount of CNT clumping appears similar between each transfer method.

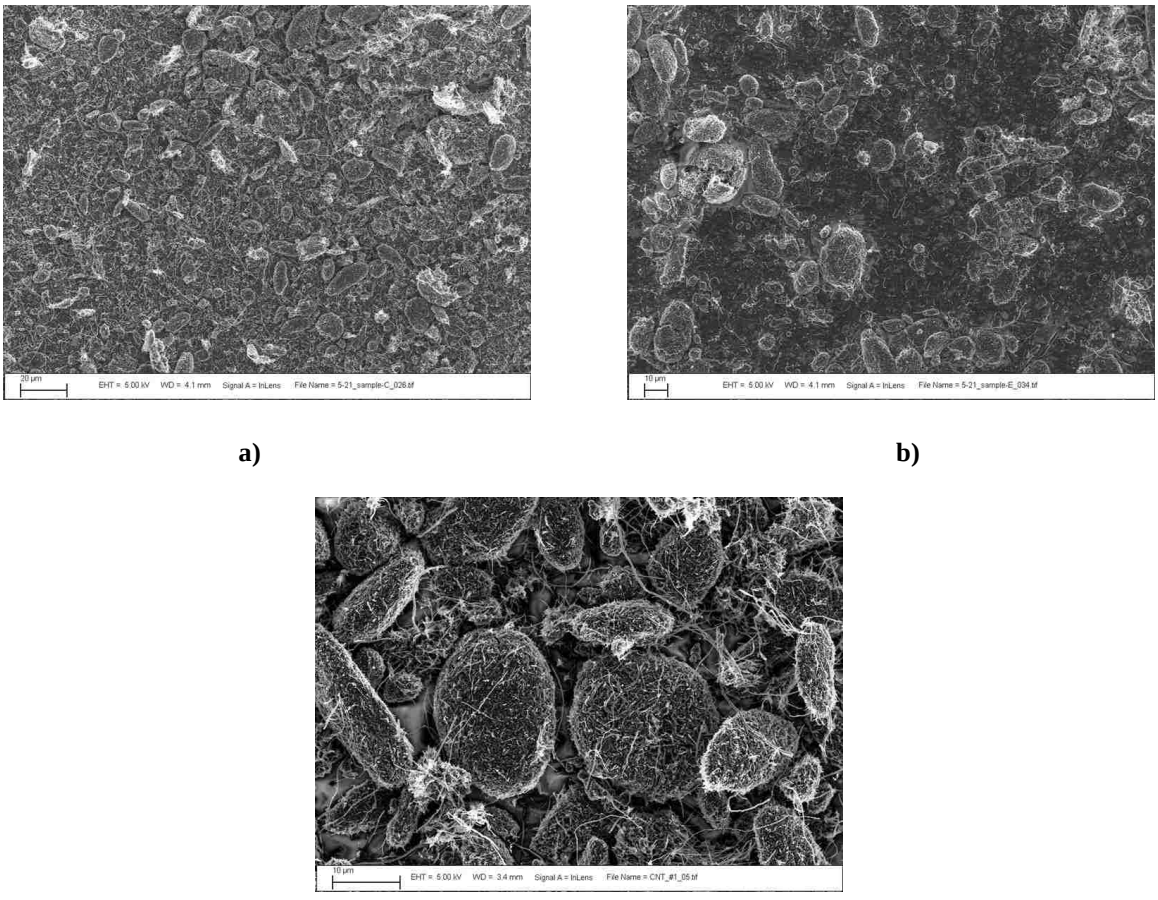

a) **b)**

c)

Figure 13. SEM images for two samples. a) shows a sample with an area density of 0.005413 kg/m^2. b) shows a sample with an area density of 0.002941 kg/m^2. c) shows a close-up of the CNT spheres

Beigbeder et al. [37] looked at the percolation threshold of a CNT/PDMS composite where the CNTs were added to the bulk of the PDMS. They plotted the conductivity of the composite as a function of CNT weight percentage and found a percolation threshold at 0.03 weight percent CNTs, and a critical volume fraction at 0.1 weight percent of CNTs. However, as can be seen in Figure 14, the conductivity of the samples from this study are much higher than from Beigbeder et al. [37], where the CNTs were added throughout the volume of the samples. The highest conductivity that Beigbeder et al. [37] recorded was $1 \cdot 10^{-6}$ S/cm at 1 weight percent CNT loading. This compares to 1368.51 S/cm, recorded at a weight percent CNT loading of 0.0833 percent in this study. This is approximately 200% higher than recorded by Beigbeder et al. [37] at a much lower loading percent of CNTs.

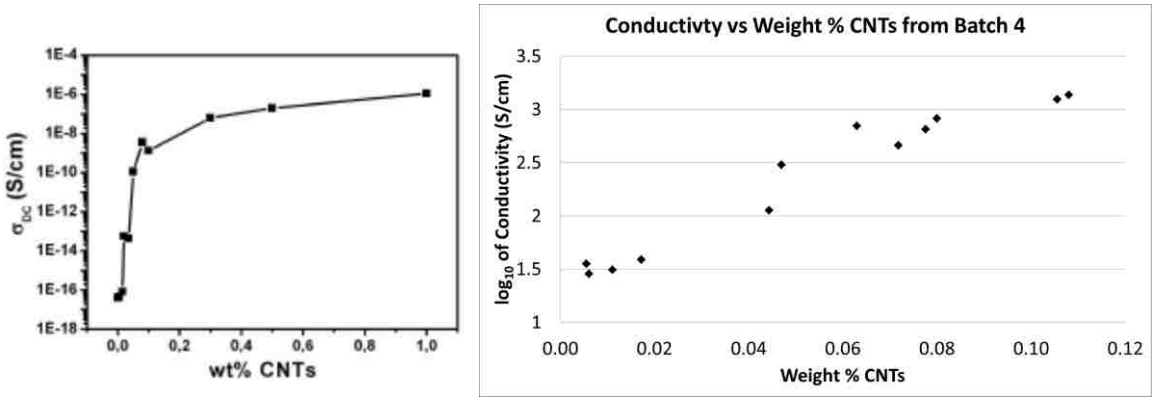

a) **b)**

Figure 14. Conductivity versus weight percent of CNTs. a) is from Beigbeder et al. [37] and b) is from this work

Wu et al. [16] also performed a study of the initial resistivity as function of CNT weight percentage from samples ranging from 1 to 4 weight percent of CNTs. As can be seen in Figure 15, the resistivity reported was much higher than in the surface-stamped

composites used in this work. The lowest resistivity recorded by Wu et al. was $1 \cdot 10^{12}$ at 4 weight percent CNT loading. This compares to a resistivity of 7.31E-4 Ω·cm recorded at a weight percent CNT loading of 0.0833 percent in this study. The resistivity is approximately 200% lower using a surface stamp technique at much lower CNT loadings. The superior electrical results give a good indication that adding CNTs to the surface of the PDMS is preferable for a microvalve membrane for electrostatic actuation. Comparison with the studies from Beigbeder et al. [37] and Wu et al. [16] supports the hypothesis that surface-stamped CNTs cause a much more conductive composite than bulk added CNTs.

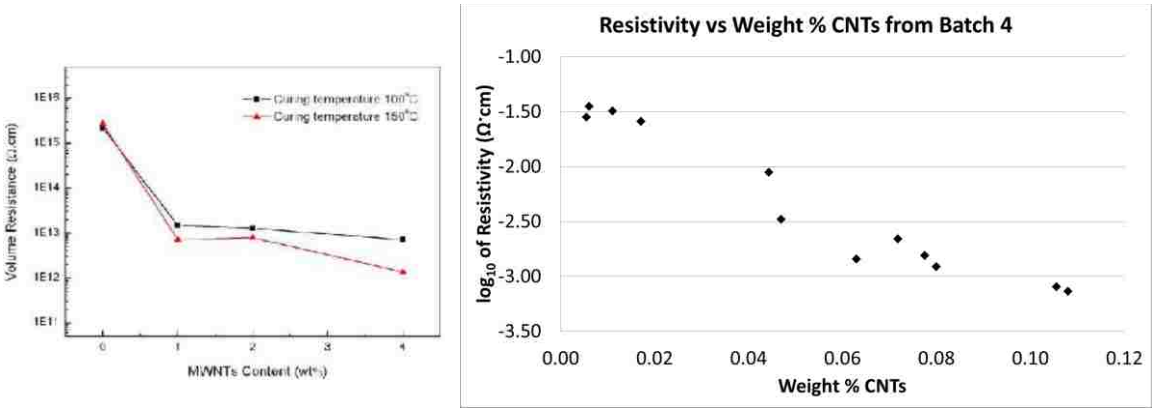

Figure 15. Resistivity versus weight percent of CNTs. a) is from Wu et al. [16] and b) is from this work

4. Conclusion

This thesis focused on the mechanical and electrical properties of a surface embedded PDMS/CNT composite as a proof of concept for a microfluidic microvalve. Results indicate that the amount of CNTs surface stamped onto PDMS have negligible effects on the mechanical properties of the composite, while having significant effects on the electrical properties. The initial resistance and change in resistance per strain is lower in samples with higher area densities of CNTs. SEM images of samples support the hypothesis that samples with a greater amount of CNTs have more pathways in which current can travel. Surface stamping the CNTs on the PDMS also results in a much higher conductivity when compared to samples with CNTs added to the bulk of the PDMS. The initial resistance of the composites was also within the range of bulk powders of carbon and MWCNTs. A low change in mechanical properties while still having good conductivity is important from a microvalve membrane standpoint because it allows for actuation with the most compliant membrane. While a surface-stamped CNT/PDMS composite appears to be a promising way to achieve a conductive microvalve membrane, further research needs to be done to understand the effects of cyclic loading on the CNT orientation as well as their ease of incorporation into microfluidic systems.

Appendices

Appendix A – Preliminary PDMS and Composite Sample Preparation

As discussed in the Introduction, a PDMS/CNT composite is being explored for use as a high displacement microvalve membrane that is easy to integrate in microfluidic systems. The most straightforward method to make a PDMS/CNT composite is to mix the CNTs directly into the bulk of the PDMS. However, due to PDMS acting as an electric insulator, the percolation threshold to achieve conduction is quite high, and requires a high weight percentage of CNTs to be added to the PDMS matrix. However, the high amount of CNTs needed for conduction also considerably strengthens and stiffens the composite. In terms of microvalve actuation, it is desirable to have the most compliant membrane possible so that the least amount of energy is required to achieve actuation. A PDMS/CNT composite with mechanical properties similar to that of pure PDMS, while still being electrically conductive, is therefore preferable. Several composite preparation techniques were therefore explored to try and achieve this.

Initial Preparation Technique

The first technique explored consisted of inserting a layer of CNTs between two layers of PDMS: a 1.5 mm thick layer and a thin film. The thin layer of PDMS was prepared by spin-coating PDMS (20:1 ratio of base to crosslinker ratio) onto a silicon wafer at 5000-7000 revolutions per minute. This gave a PDMS layer approximately 10-20 µm thick. The silicon wafer with the PDMS was then semi-cured in an oven at 70^{o}C for 45 minutes, stamped with a CNT filter (see Experimental section for preparation), and then stamped onto a semi-cured PDMS sample (approximately 1.5 mm thick, 5:1 base to crosslinker ratio). The different mixing ratios of the PDMS layers helped with

crosslinking between the layers (through the thin CNT layer) so that the two layers of PDMS could stick together as a single composite. While different mixing ratios of base to crosslinker can cause different mechanical properties in the PDMS, it was believed that the different PDMS layers would not cause the composite to become stiffer on one side due to the thinness of one of the PDMS layers. The resulting composite sample was then fully cured in the oven at 70^{o}C for 1.5 hours. The PDMS was then peeled off of the silicon wafer, resulting in a layer of PDMS, CNT, and thin layer of PDMS. Figure 16 shows a cross-sectional image of the composite.

The composite was then stamped into the dogbone tensile testing shape, and mounted to the custom tension testing robot in the same fashion as described in the Experimental section. In order to record resistance, the samples were pierced all the way through with gold wire. This method was abandoned due to lack of consistency between samples. Often, the thin layer of PDMS would tear during the peeling process or the dogbone stamping process. It was also difficult to get an approximation of the weight of the carbon nanotubes due to the CNT layer being stamped before the samples were stamped into the dogbone shape.

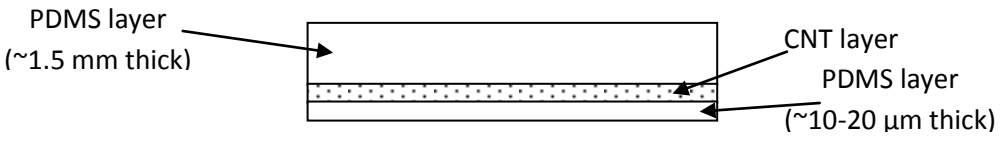

Figure 16. Cross-section of thin-layered CNT sandwiched composite.

Second Preparation Technique

A similar preparation technique was utilized next, in which the CNT layer was stamped between two layers of PDMS, each of the same thickness. The PDMS layers were prepared by pouring the PDMS (10:1 ratio base to crosslinker ratio) in a wax mold, approximately 1.5 mm thick, and semi-curing in an oven at 70^{o}C for 1 hour. The samples were then stamped into the dogbone tensile testing shape, weighed, and stamped with the CNT filter as described above. The samples where re-weighed and placed back in the oven for an additional 1.5 hours at 70^{o}C to fully cure. Figure 17 shows a cross-sectional image of the composite.

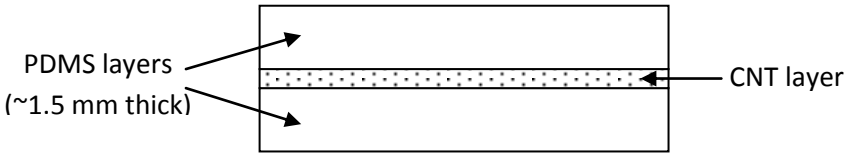

Figure 17. Cross-section of CNT sandwiched composite.

Unlike with the initial preparation method, the two layers of PDMS in this method used the same base to crosslinker mixing ratio in each of the two PDMS layers. As discussed in Initial Preparation Technique section, while using different mixing ratios can help promote crosslinking between the different PDMS layers, it can have a significant effect on the mechanical properties of PDMS layers. In this case, because the two layers of PDMS are the same thickness, a difference in stiffness of one layer would cause an un-symmetric composite in terms of stiffness. During tension testing, the stiffer layer would take a larger force to strain, causing the sample to have both a bending and axial force applied. This could result in the stress and strain calculations to be inaccurate. For this

reason, the two layers have the same base to crosslinker mixing ratio, even though this is less conductive to crosslinking between the PDMS layers.

This method had several problems. The first problem occurred in samples of pure PDMS (with no CNT layer) occasionally de-laminating into two layers after they had been cured together. This de-lamination would occur during tension testing, and would result in the sample breaking in two different locations. An example of this can be seen in Figure 18.

Figure 18. Example of de-lamination that occurred during tension testing.

This would also cause problems with stress and strain calculations, and cause inconsistencies and lack of repeatability in the samples. A plot of the stress-strain results after a sample broke in two different locations after de-lamination can be seen in Figure 19. As the sample was strained, the two layers of PDMS de-laminated from each other, and one layer broke first. This is represented on the graph in the small jump in stress at

around 350% strain. The sample continued to be strained, but was now half as thick as it originally was at the beginning of the tension test.

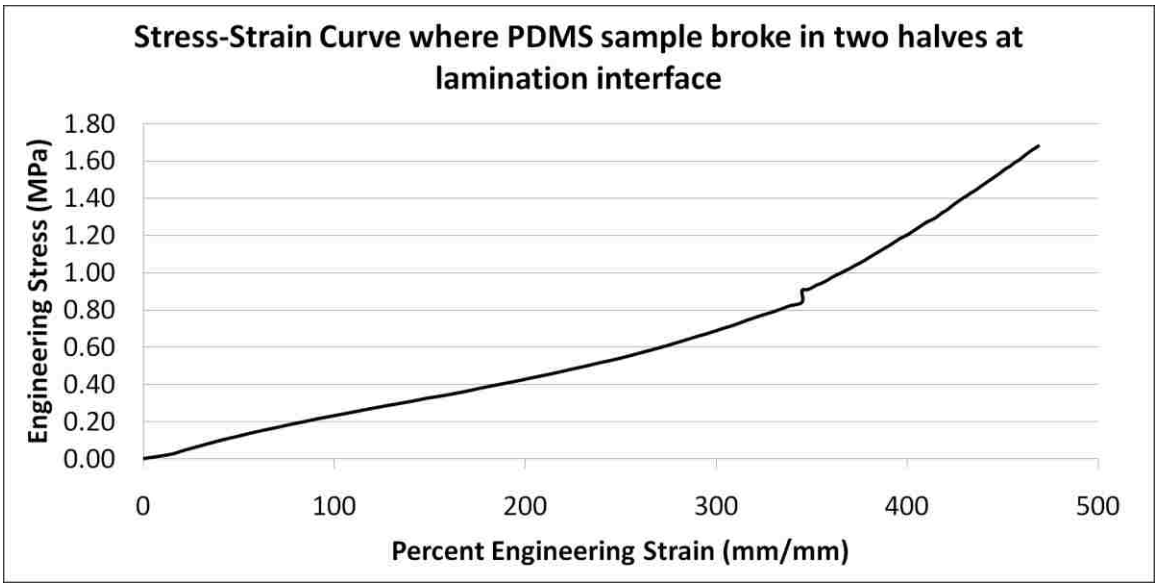

Figure 19. Stress-strain curve where dogbone sample broke in two halves

Another problem occurred when the layer of CNTs were applied between the two layers of PDMS. In these samples, there was difficulty in getting the two layers to PDMS to cure together between the CNT layer. The crosslinker of the PDMS could not effectively permeate between the CNT layer, frequently resulting in the two PDMS layers to not bonding together. This resulted in the PDMS only sticking together at the top and bottom of the sample, where CNTs were not stamped. This effectively resulted in the composite acting as two separate samples during tension testing.

A third problem was a difficultly in achieving consistent resistance readings using the 4 point measurement. This was due to the gold wire needing to be pierced through the sample in order to interact with the CNT layer. This not only made it difficult to read the

resistance readings consistently due to the small area of contact, but piercing the sample also resulted in a stress concentration, causing some samples to break at the gold wire interface during tension testing.

Current Preparation Technique

The current preparation technique eliminates one of the layers of PDMS used in the second preparation technique. The PDMS/CNT composite is therefore consists of a layer of PDMS with a thin layer of CNTs on top, as seen in Figure 20. The sample preparation is explained in the Experimental section. Because the CNT layer is now on the outside of the composite, the gold wire does not have to pierce through the sample, and eliminates the stress concentration that this caused. The gold wire was therefore flattened and placed in between the CNT layer and the machine grips. The larger contact area of the flattened gold wire made for more consistent resistance measurements.

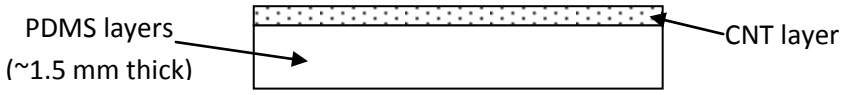

Figure 20. Cross-section of the current composite.

Appendix B – Mechanical Testing Design Iterations and Results

Several design iterations were performed on the dogbone tension shape and the machine grips that hold the sample in place throughout the displacement. ASTM D412, the standard test methods for vulcanized rubber and thermoplastic elastomers in tension, was referenced by others in literature and used as the basis for the dogbone shapes used in this work. Figure 21 shows an example of two different dogbone shapes used in literature, each of which referenced the ASTM D412 standard. Figure 21 gives an indication of the large variations that can exist between the dimensions of the dogbones in the ASTM standard.

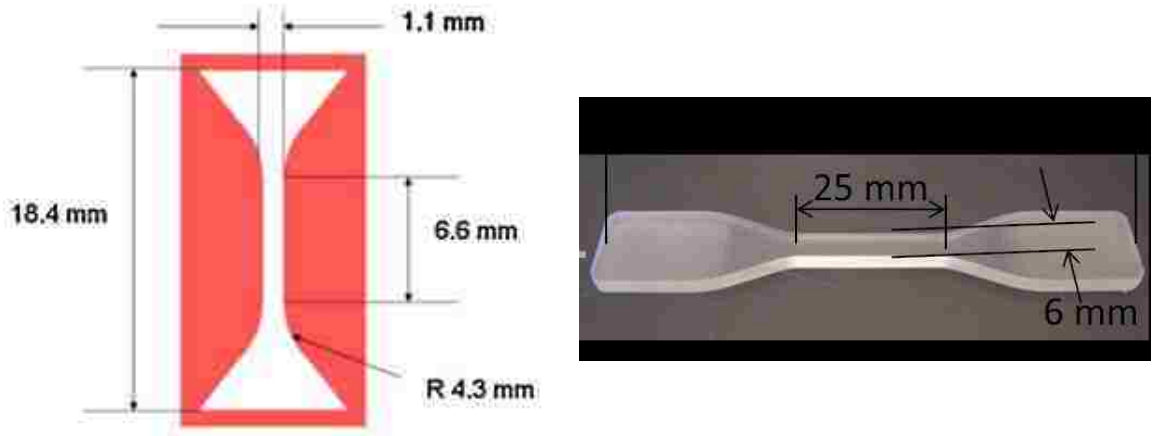

a) **b)**

Figure 21. Two dogbone shapes used in literature. a) is the dogbone used by Liu et al. [11] b) is the dogbone used by Khanafer et al. [14]

Initial Dogbone Design (Dogbone Design #1)

The initial dogbone shape and its dimensions can be seen in Figure 22. During tension testing, this dogbone shape consistently broke along the radius which transitions into the gauge width, as can be seen in Figure 22 b). This indicates that there is a stress

concentration occurring at this transition, causing the samples to break here instead of along the gauge width. This caused inaccuracies in the cross-sectional area used for stress calculations.

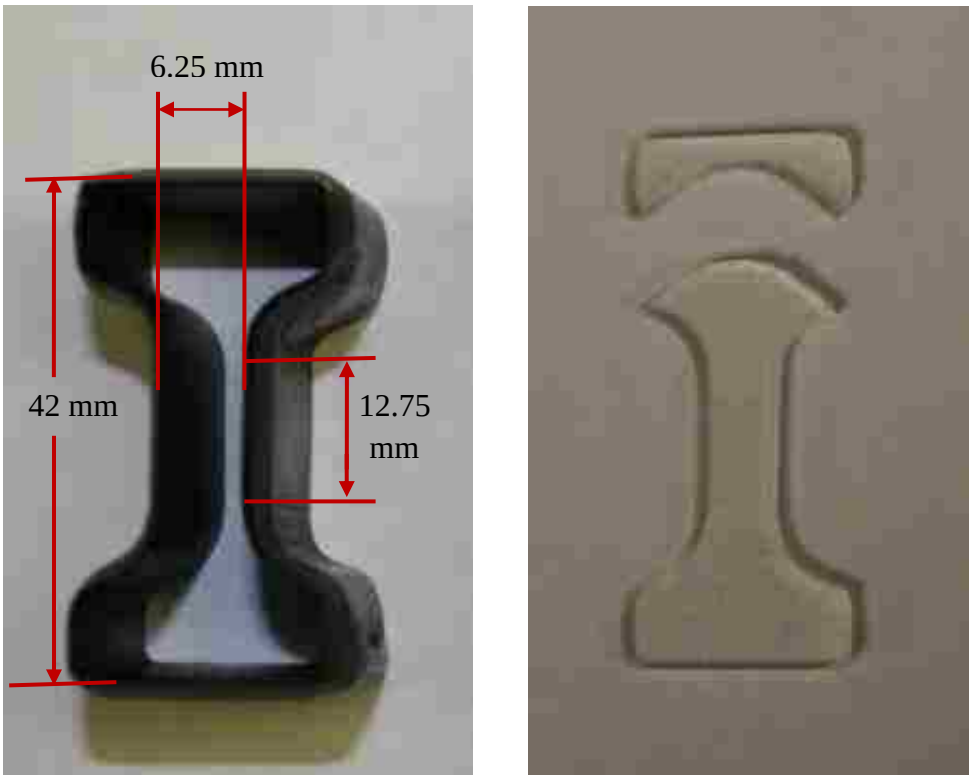

a) **b)**

Figure 22. Original dogbone shape. a) shows the dogbone dimensions. b) shows the common failure location.

Second Design Iteration of Dogbone (Dogbone Design #2)

The next dogbone iteration used an ASTM standard with a longer gauge length, narrower gauge width, and increased radius transition into the gauge width. The increased radius was utilized to try to smooth out the transition into the gauge width and eliminate the stress concentration seen at this location in dogbone design #1. The second dogbone design and its dimensions can be seen in Figure 23. As can be seen in Figure 23 b), the

samples again broke at the transition radius as well as at the grip interface, rather than along the gauge width. The stress-strain plot associated with samples from dogbone #2 can be seen in Figure 24. The four samples shown have a wide variation in their stress-strain curves. Because the samples broke outside of the gauge width, an accurate measurement of the cross-sectional area at which the samples broke could not be achieved. This, along with samples slipping in the machine grips (as described in the following section), caused the wide variation in the mechanical properties recorded. While the dogbone standards with a shorter gauge length and wider gauge width worked for others in literature, the combination of these dogbone shapes with the grips used during tension testing caused the samples to break outside of the gauge width. A dogbone shape with a longer gauge length and narrower gauge width, as well as modifications to the machine grip design, where necessary in order to achieve failure in the dogbone along the gauge width.

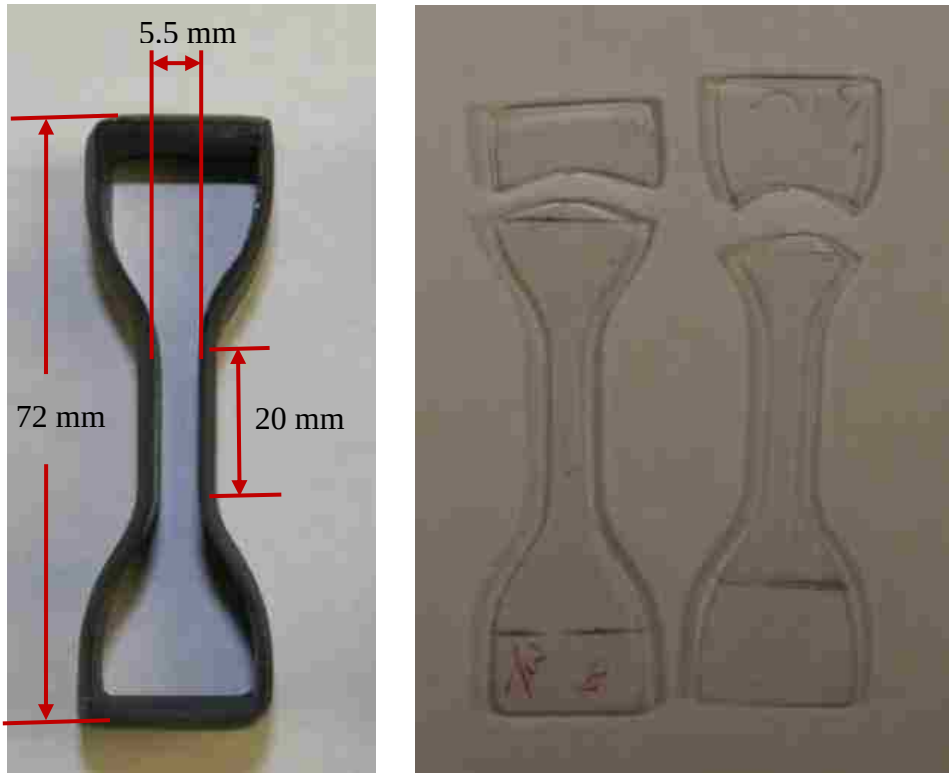

Figure 23. Second design iteration of the dogbone. a) shows the dogbone dimensions. b) shows the common failure locations.

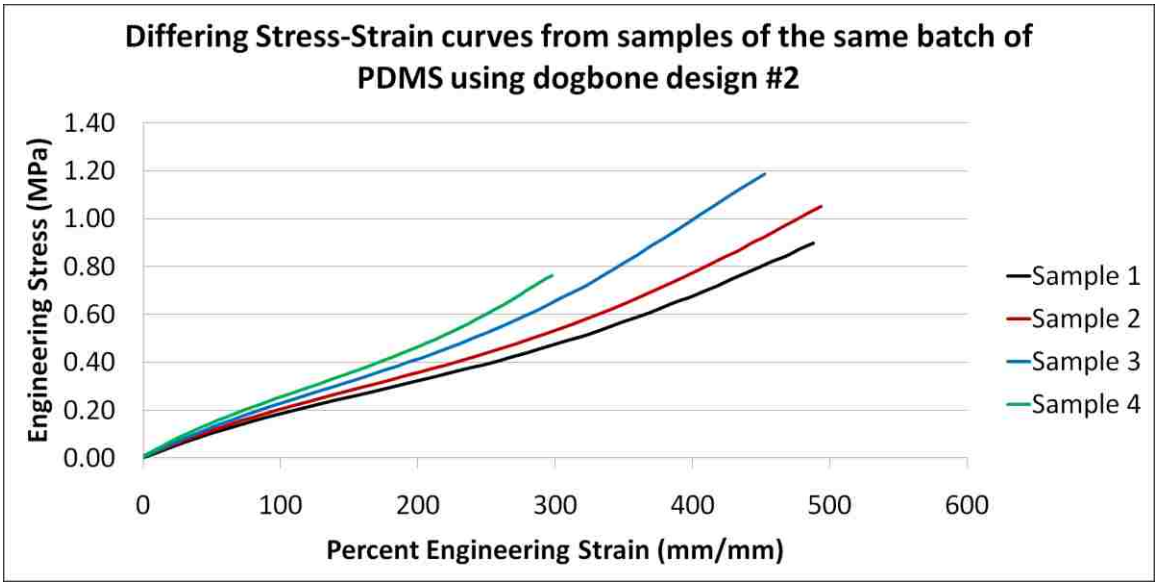

Figure 24. Stress-Strain curves showing differing mechanical properties of samples tested using dogbone design #2.

Machine Grip Design Iteration

The initial grip design can be seen in Figure 25. It had a smooth surface in which the dogbone specimens were clamped. The smooth surface of this grip design required a high clamping force to be applied to the samples in order for the samples not to slip during displacement. The high clamping force necessary created a stress concentration along the grip interface, causing some samples to break at this location. However, at higher strains some samples still slipped in the grip, even with the high clamp force applied. This caused inaccuracies in the strain calculations, especially at higher strain rates, where sample slip was more prevalent. Figure 26 shows a stress-strain plot where one of the samples slipped (Sample 4). As can be seen, Sample 4 closely follows the stress-strain profile up to about 180% strain, as indicated by the dashed vertical line. At this point, the sample begins to slip in the machine grip. As the sample slips, the force recorded by the load cell decreases, and inaccurate mechanical properties are recorded.

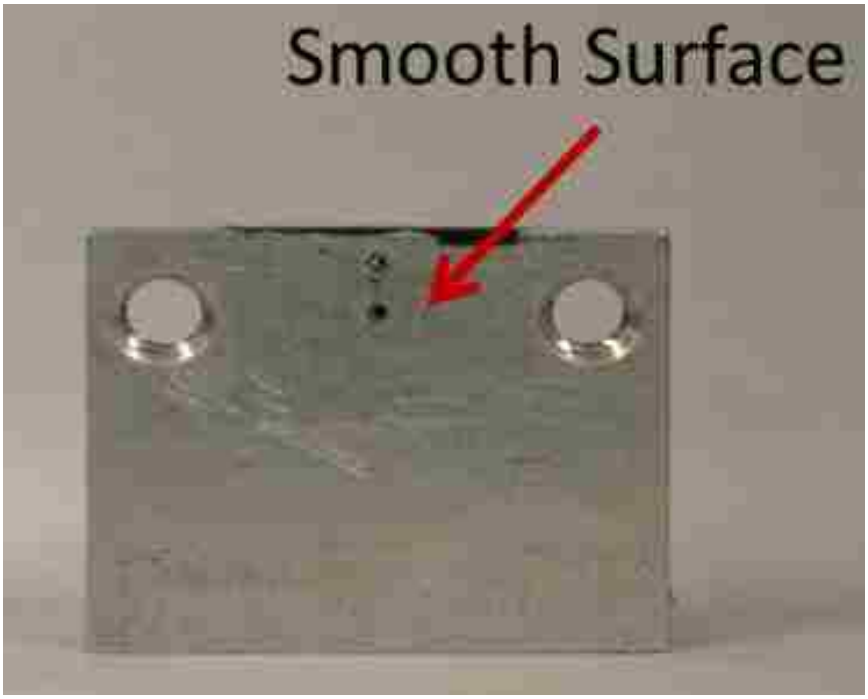

Figure 25. Initial grip design with smooth interface.

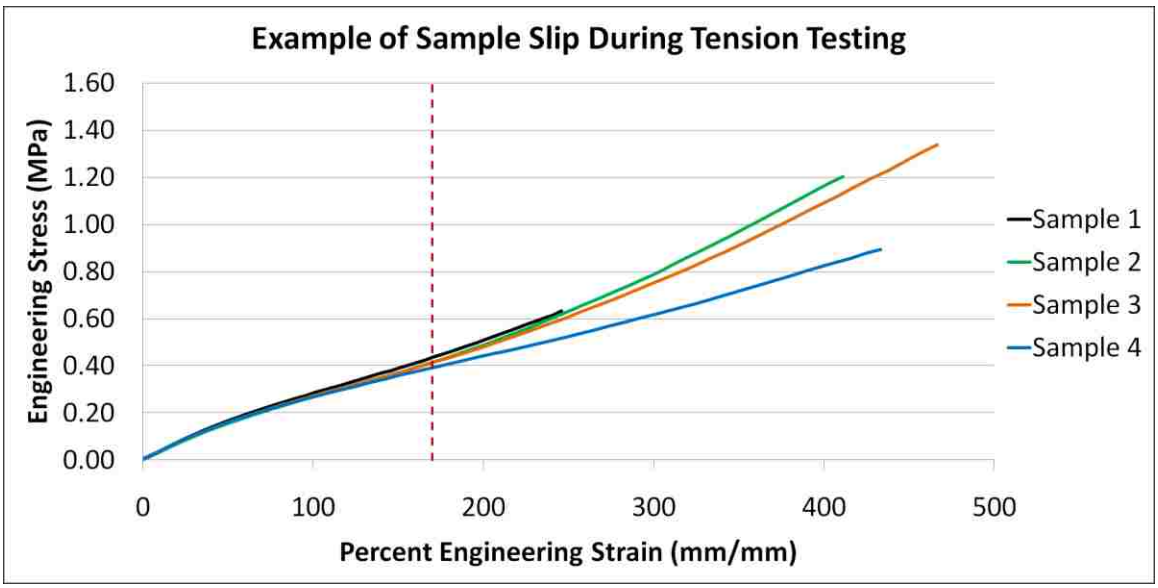

Figure 26. Example of sample slip in Sample 4 during strain. The red dashed line indicates where the sample began to slip.

A knurled surface was added to the interface to help grip the samples and decrease the clamping force applied to the samples. This reduced the stress concentration at the grip interface, but caused the knurled surface to cut into the PDMS. Again, this caused the samples to break along the damaged surface, instead of along the gauge width. Design iterations to the sample preparation technique were being performed (as described in Appendix A) while the grip design was being modified. Because the new preparation technique had the CNTs surface-stamped onto the PDMS, the grip interface had to be modified so that the samples would be electrically isolated from the rest of the system for resistance measurements. A rubber interface was applied to the knurled grip interface that comes in contact with the CNT layer. This not only served to electrically isolate the samples, but further helped grip the samples and prevented the knurled surface from cutting into the PDMS. The modified grip design with knurled surface and rubber interface can be seen in Figure 27.

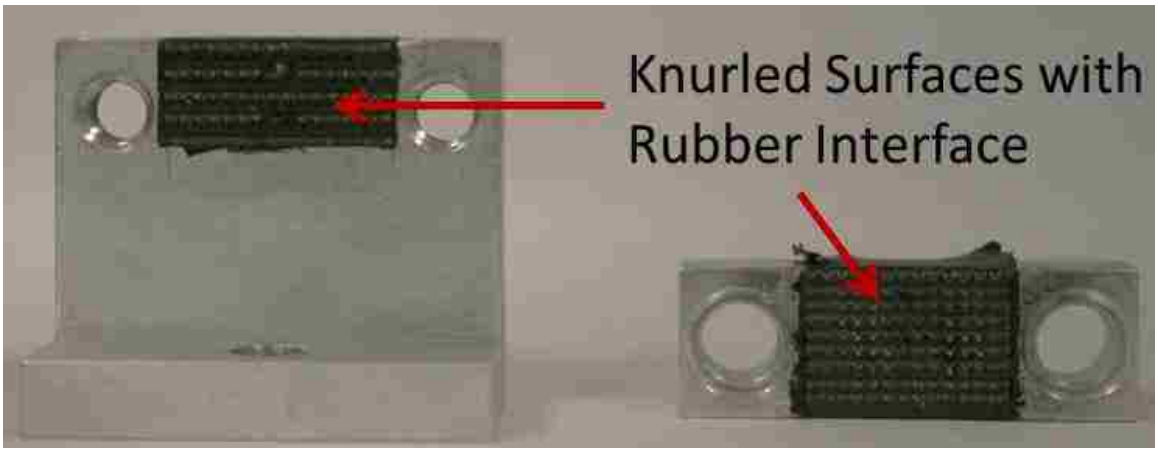

Figure 27. Grip design with knurled surface and rubber interface.

Final Design of Dogbone (Dogbone Design #3)

Figure 28 shows the final design iteration of the dogbone. An ASTM standard with a longer gauge length and narrow gauge width, along with the modifications to the machine grips, was found to eliminate the stress concentrations along the transition radius that was prevalent in the early dogbone iterations. Figure 28 b) shows examples of common failure points using this dogbone shape.

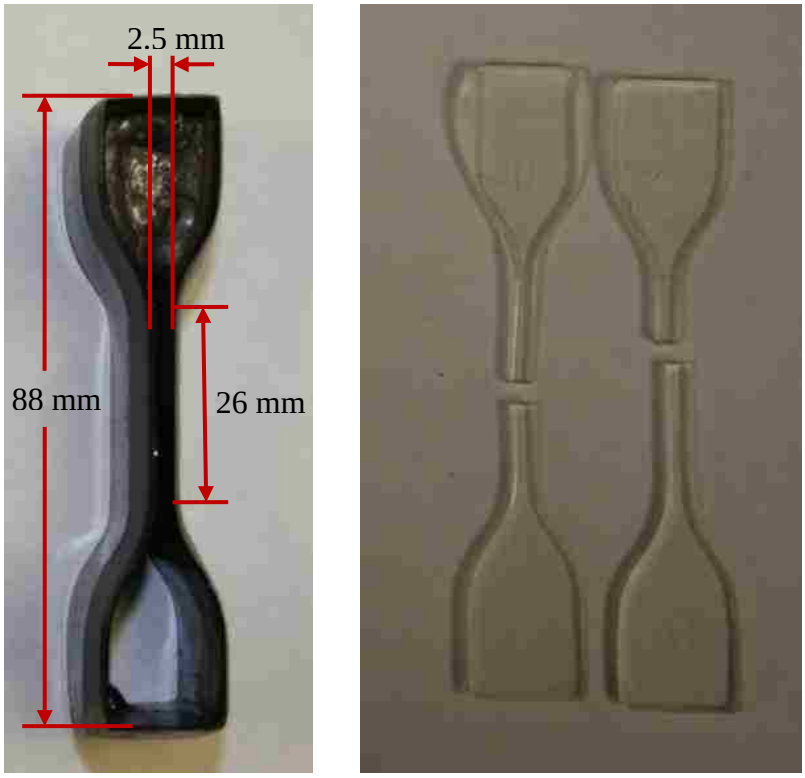

Figure 28. Final design iteration of the dogbone. a) shows the dogbone dimensions. b) shows the common failure locations.

Appendix C – SEM Images of Three Different CNT Transfer Methods

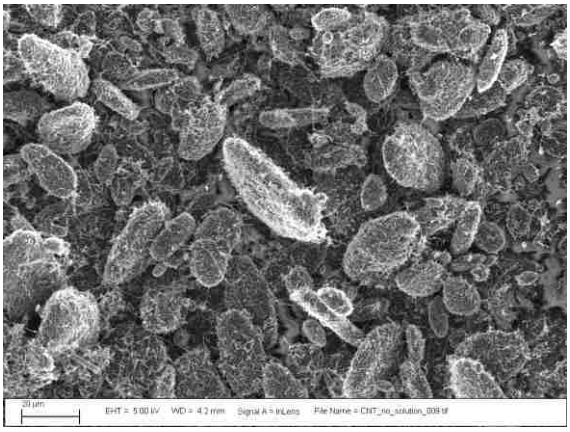

CNTs Direct Transfer Method

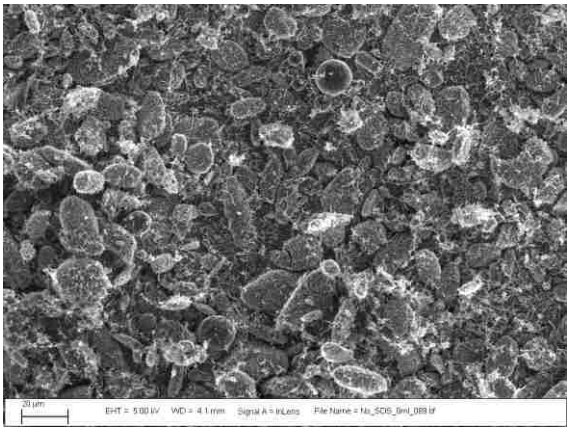

CNT Solution with no SDS Transfer Method

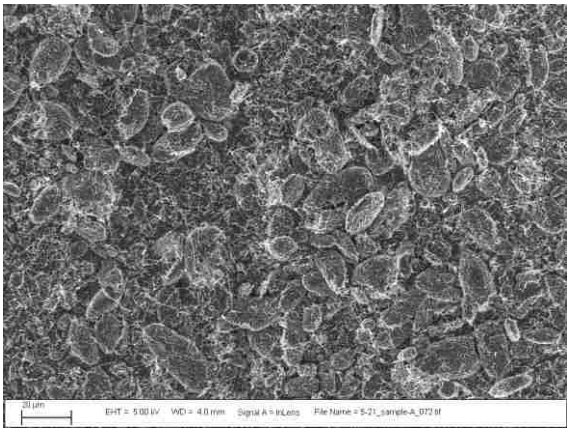

CNT Solution with SDS Transfer Method

Appendix D – Equations

Elastic modulus of the CNTs in the longitudinal direction:

$$E_{f1} = 1000\ GPa$$

Elastic modulus of the CNTs in the transverse direction:

$$E_{f2} = 1000\ GPa$$

Elastic modulus of the PDMS:

$$E_m = 0.00042\ GPa$$

Approximate area of the dogbone stamp:

$$A = 807.31\ mm^2$$

Approximate thickness of the PDMS layer:

$$t_m = 1.5\ mm$$

Approximate thickness of the CNT layer:

$$t_f = 7.5E(-6)\ mm$$

Approximate volume of the PDMS layer:

$$v_m = A * t_m = 807.31 * 1.5 = 1210.965\ mm^3$$

Approximate volume of the CNT layer:

$$v_f = A * t_f = 807.31 * 7.5E(-6) = 0.00605\ mm^3$$

Approximate total volume of the composite:

$$v_c = v_m + v_f = 1210.97105\ mm^3$$

Volume fraction of PDMS:

$$V_m = \frac{v_m}{v_c} = \frac{1210.965}{1210.97105} = 0.999995$$

Volume fraction of CNTs:

$$V_f = V_p = \frac{v_f}{v_c} = \frac{0.00605}{1210.97105} = 0.000005$$

Length of CNT perpendicular to the applied load:

$$L = 7.5\ nm = 7.5E(-6)\ mm$$

Length of CNT parallel to the loading direction:

$$t = 7500\ nm = 0.0075\ mm$$

Basic Rule of Mixtures in the longitudinal direction:

$$E_{c1} = E_{f1}V_f + E_mV_m$$

$$E_{c1} = 1000(0.000005) + 0.00042(0.999995) = 0.00542\ GPa = 5.42\ MPa$$

Basic Rule of Mixtures in the transverse direction:

$$1/E_{c2} = V_f/E_{f2} + V_m/E_m$$

$$1/E_{c2} = \frac{0.000005}{1000} + \frac{0.999995}{0.0042} = 2380.94\ GPa$$

$$E_{c2} = \frac{1}{2380.94} = 0.00042\ GPa = 0.42\ MPa$$

Tsai and Pagano modified Rule of Mixtures for randomly oriented discontinuous fibers:

$$\tilde{E}_c = 3/8\ (E_1) + 5/8\ (E_2)$$

$$\tilde{E}_c = \frac{3}{8}(5.42) + \frac{5}{8}(0.42) = 2.0325 + 0.2625 = 2.295\ MPa$$

Fukuda & Chou and Nardone & Prewo particulate reinforced composite modulus:

$$E_c = E_m[1 + (L + t)/4L]V_p + E_m\big(1 - V_p\big)$$

$$E_c = 0.00042\left[1 + \frac{(7.5E(-6) + 0.0075)}{4\big(7.5E(-6)\big)}\right]0.000005 + 0.00042(1 - 0.000005)$$

$$E_c = 0.4205\ MPa$$

Appendix E – Codes

MATLAB code used to apply a Gaussian kernel regression to the inputted data:

```
function [k_x,f] = kernf(x,y,h,N)

% Gaussian kernel smoothing regression
%
% [k_x,f]=kernf(x,y,h,N) returns the Gaussian kernel regression such that
%   f(k_x) = y(x) + e
%
% h is the bandwidth
% N is the number of regression points to use
%
% Algorithm
% The kernel regression is a non-parametric approach to estimate the
% conditional expectation of a random variable:
%
% E(Y|X) = f(X)
%
% where f is a non-parametric function. Based on the kernel density
% estimation, this code implements the Nadaraya-Watson kernel regression
% using the Gaussian kernel as follows:
%
% f(X) = sum(kern((x-X)/h).*Y)/sum(kern((x-X)/h))

x = x(:);   % Puts the x-data in a vector
y = y(:);   % Puts the y-data in a vector

kern = @(z) exp(-z.*z/2)/sqrt(2*pi);    % Gaussian kernel function

k_x = linspace(min(x),max(x),N);   % Generates a linearly spaced vector N points
                                   % between the min and max values of x vector
f = zeros(1,N); % Creates a vector of zeroes of length N

for k=1:N   % Executes a loop N times
    z=kern((k_x(k)-x)/h);   % Solves the Gaussian kernel function for each k_x value
    f(k)=sum(z.*y)/sum(z);  % Solves the Nadaraya-Watson regression equation
end

k_x = k_x(:);   % Puts the k_x into a vector
f = f(:);       % Puts the f data into a vector
```

LabVIEW code used to record the data from the load cell and mulimeter:

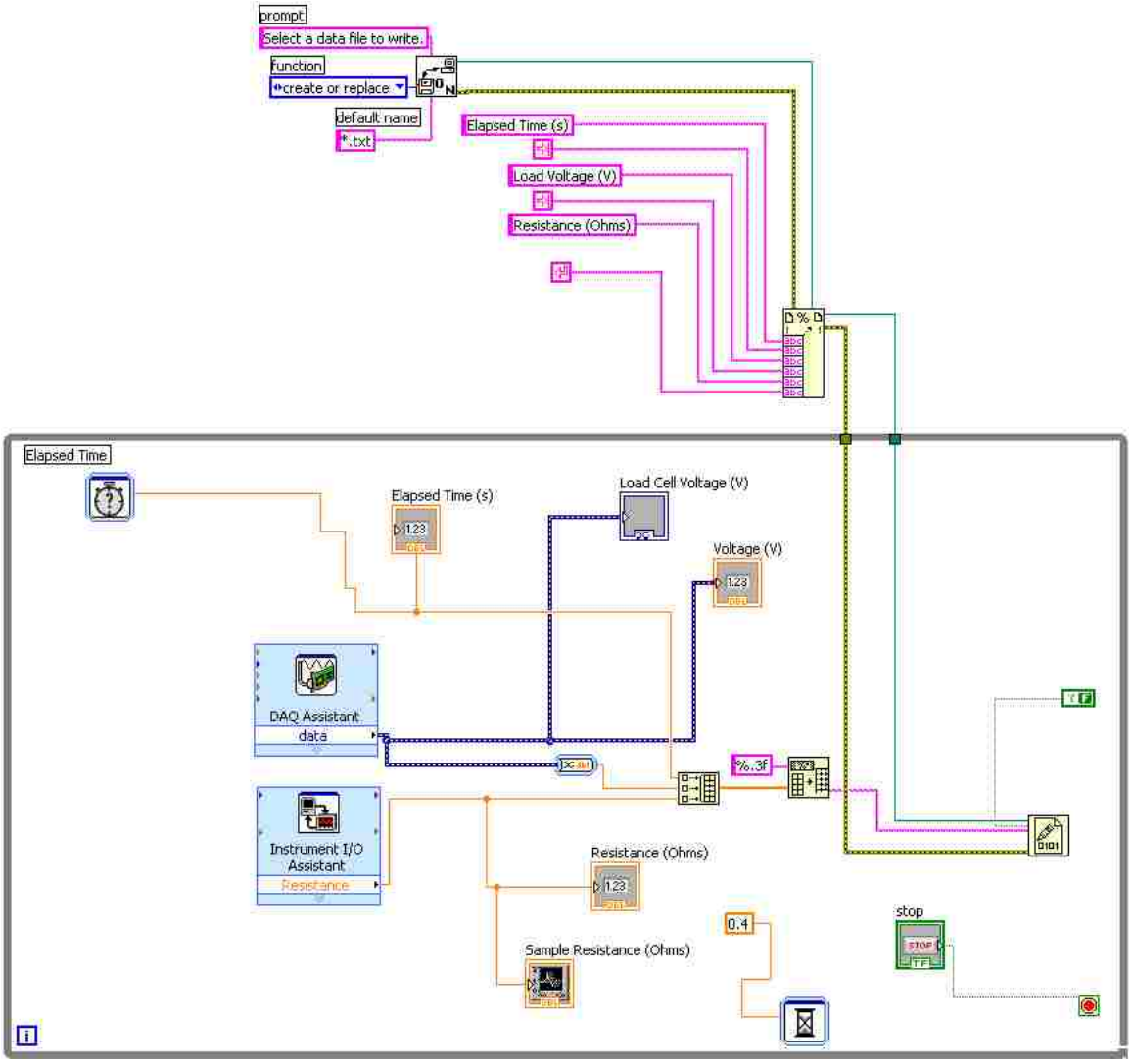

The user interface of the LabVIEW code:

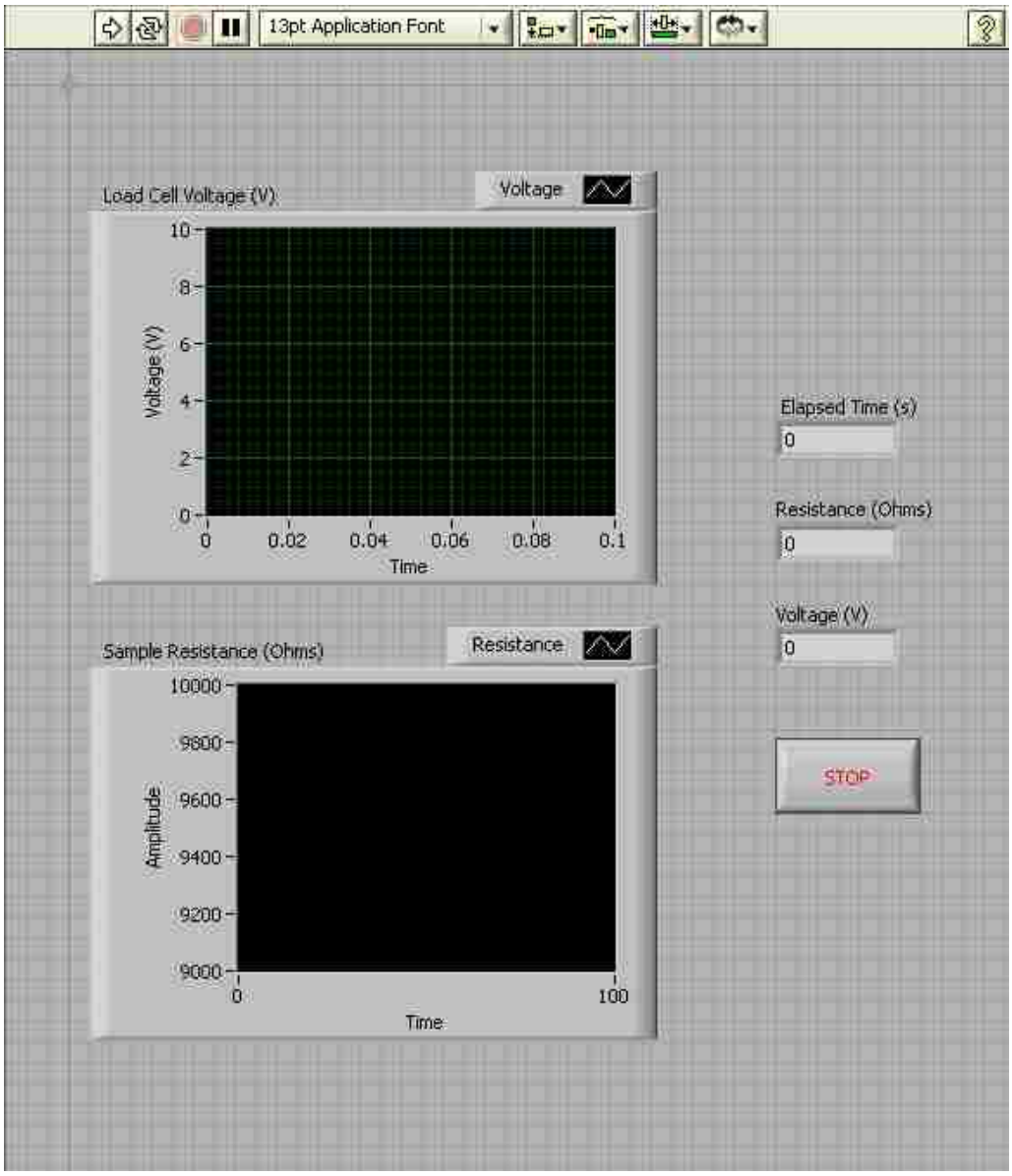

References

[1] K.W. Oh, C.H. Ahn, A Review of Microvalves, J. Micromech. Microengineering 16 (2006) R13-R39.

[2] N. Jeon, D. Chiu, C. Wargo, H. Wu, I. Choi, J. Anderson, G. Whitesides, Design and Fabrication of Integrated Passive Valves and Pumps for Flexible Polymer 3-Dimensional Microfluidic Systems, Biomedical Microdevices 4 (2002) 117-121.

[3] K. Hosokawa, R. Meada, Pneumatically-actuated three-way microvalve fabricated with polydimethylsiloxane using the membrane transfer technique, J. Micromech. Microengineering 10 (2000) 415-420.

[4] V. Studer, G. Hang, A. Pandolfi, M. Ortiz, A.W. French, S.R. Quake, Scaling properties of a low-actuation pressure microfluidic valve, J. Appl. Phys. 95 (2004) 393-398.

[5] S.W. Lee, D.J. Kim, Y. Ahn, Y.G. Chai, Simple structured polydimethylsiloxane microvalve actuated by external air pressure, Proc. Inst. Mech. Eng. Part C J. Mech. Eng. Sci. 220 (2006) 1283-1288.

[6] D. Beigelsen, A. Berlin, P. Cheung, M. Fromherz, D. Goldberg, W. Jackson, B. Preas, J. Reich, L. Swartz, AirJet paper mover: An example of meso-scale MEMS, Proc. SPIE Int. Soc. Opt. Eng. 4176 (2000) 122-129.

[7] T.K. Chuang, M. Troccoli, P.C. Kuo, A. Jamshidi-Roubari, M.K. Hatalis, I. Biaggio, A.T. Voutsas, Top-emitting 230 dots/in. active-matrix polymer light-emitting diode displays on flexible metal foil substrates, Appl. Phys. Lett. 90 (2007).

[8] C.X. Liu, J.W. Choi, Patterning conductive PDMS nanocomposite in an elastomer using microcontact printing, J. Micromech. Microengineering 19 (2009) 1-7.

[9] D. Kim, J.E. Han, H. Park, K.S. Yun, Simple and low-cost patterning of carbon nanotube on PDMS for flexible MEMS, Int. Solid-State Sensors, Actuators Microsystems Conf., (2011) 2355-2358.

[10] J.C. McDonald, G.M. Whitesides, Poly(dimethylsiloxane) as a material for fabricating microfluidic devices, Acc. Chem. Research 35 (2002) 491-499.

[11] M. Liu, J. Sun, Q. Chen, Influences of heating temperature on mechanical properties of polydimethylsiloxane, Sens. and Actuators A Phys 151 (2009) 42-45.

[12] D.B. Weibel, M. Kruithof, S. Potenta, S.K. Sia, A. Lee, G.M. Whitesides, Torque-actuated valves for microfluidics, Anal. Chem. 77 (2005) 4726-4733.

[13] B. Samel, J. Melin, P. Griss, G. Stemme, Single-use microfluidic pumps and valves based on a thermally responsive PDMS composite, Proc. IEEE Int. Conf. Micro Electro Mech. Syst. MEMS (2005) 690-693.

[14] K. Khanafer, A. Duprey, M. Schlicht, R. Berquer, Effects of strain rate, mixing ratio, and stress-strain definition on the mechanical behavior of the polydimethylsiloxane (PDMS) material as related to its biological applications, Biomed. Microdevices 11 (2009) 503-508.

[15] C.L. Wu, H.C. Lin, J.S. Hsu, M.C. Yip, W. Fang, Static and dynamic mechanical properties of polydimethylsiloxane/carbon nanotube nanocomposites, Thin Solid Films 517 (2009) 4895-4901.

[16] C.L. Wu, H.C. Lin, C.H. Huang, M.C. Yip, W. Fang, Mechanical properties of PDMS/CNTs nanocomposites, Mater. Res. Soc. Symp. Proc. 1056 (2008) 84-89.

[17] S. Iijima, Helical microtubules of graphitic carbon, Nature 354 (1991) 56.

[18] J. Paul, S. Sindhu, M.H. Nurmawati, S. Valiyaveettil, Mechanics of prestressed polydimethylsiloxane-carbon nanotube composite, Appl. Phys. Lett. 89 (2006).

[19] R.B. Mathur, S. Pande, B.P. Singh, T.L. Dhami, Electrical and mechanical properties of multi-walled carbon nanotubes reinforced PMMA and PS composites, Polym. Compos. 29 (2008) 717-727.

[20] K. Ahmad, W. Pan, Dramatic effect of multiwalled carbon nanotubes on the electrical properties of alumina based ceramic nanocomposites, Compos. Sci. Technol. 69 (2009) 1016-1021.

[21] S. Roy, N.G. Sahoo, M. Mukherjee, C.K. Das, S.H. Chan, U. Li, Improvement of properties of polyetherimide/liquid crystalline polymer blends in the presence of functionalized carbon nanotubes, J. Nanosci. Nanotechnol. 9 (2009) 1928-1934.

[22] Handbook of Chemistry and Physics, 61st ed., CRC Press, 1974.

[23] R. Mohan, B.R. Shudel, A.V. Desai, J.D. Yearsley, C.A. Apblett, P.J. Kenis, Design considerations for elastomeric normally closed microfluidic valves, Sens. Act. B Chem. (2011), in press.

[24] ASTM, ASTM D412, Standard test methods for vulcanized rubber and thermoplastic elastomers – tension (2011), Available from: http://wwww.astm.org/cgi-bin/SoftCart.exe/STORE/showcart.html?A+mystore+opcn3581+PDF-D412+1203970149.

[25] J.S. Simonoff, Smoothing Methods in Statistics, Springer-Verlag New York, Inc., New York, 1996.

[26] E.A. Nadaraya, On Estimating Regression, Theory of Probability and its Applications 9 (1964).

[27] W.D. Callister, D.G. Rethwisch, Materials Science and Engineering: An Introduction, 8th ed., John Wiley and Sons, Inc., New Jersey, 2010.

[28] W.F. Smith, J. Hashemi, Foundations of Materials Science and Engineering, 4th ed., McGraw-Hill, New York, 2006.

[29] R.F. Gibson, Principles of Composite Material Mechanics, McGraw-Hill, New York, 1994.

[30] E.W. Wong, P.E. Sheehan, C.M. Lieber, Nanobeam mechanics: Elasticity, strength, and toughness of nanorods and nanotubes, Science 277 (1997) 1971-1975.

[31] M.M.J. Treacy, T.W. Ebbesen, J.M. Gibson, Exceptionally high Young's modulus observed for individual carbon nanotubes, Lett. Nature 381 (1996) 678-680.

[32] P. Poncharal, Z.L. Wang, D. Ugarte, W.A. de Heer, Electrostatic deflections and electromechanical resonances of carbon nanotubes, Science 283 (1999) 1513-1516.

[33] K.K. Chawla, Composite Materials, 2nd ed., Springer, New York, 1998.

[34] P. Singjai, S. Changsarn, S. Thongtem, Electrical resistivity of bulk multi-walled carbon nanotubes synthesized by an infusion chemical vapor deposition method, Mater. Sci. Eng. A 443 (2007) 42-46.

[35] R.A. Ma, C.L. Xu, B.Q. Wei, J. Liang, D.H. Wu, D.J. Li, Electrical conductivity and field emission characteristics of hot-pressed sintered carbon nanotubes, Mater. Res. Bulletin 34 (1999) 741-747.

[36] C. Qin, X. Shi, S.Q. Bai, L.D. Chen, L.J. Wang, High temperature electrical and thermal properties of the bulk carbon nanotube prepared by SPS, Mater. Sci. Eng. A 420 (2006) 208-211.

[37] J. Beigbeder, P. Demont, S. Remaury, P. Nabarra, C. Lacabanne, Incorporation of nanoparticles in a flexible solar reflector for geostationary applications, International Symposium on Materials in a Space Environment (2009).